Supplement of Atmos. Chem. Phys., 26, 15721–15733, 2026
https://doi.org/10.5194/acp-26-15721-2026-supplement
© Author(s) 2026. CC BY 4.0 License.



Atmospheric Chemistry and Physics
Open Access

Supplement of

Organic condensation derived from different volatility parameterizations and its implications for ambient nanoparticle growth

Chuang Li et al.

Correspondence to: Lei Yao (lei_yao@fudan.edu.cn) and Lin Wang (lin_wang@fudan.edu.cn)

The copyright of individual parts of the supplement might differ from the article licence.

Supplementary Text

S1. Detailed configuration of the laminar flow reactor

1.1 Seed-particle generation and classification

Self-charged polydisperse Ni-Cr seed nanoparticles were produced by resistive heating of a nichrome wire in clean, dry air, and subsequently classified into a monodisperse size distribution using a high-resolution half-mini differential mobility analyzer (half-mini-DMA), operated with a 5.6 L min^{-1} flow of ultra-high-purity nitrogen (99.999%) as the carrier gas. Of the monodisperse outflow, 0.6 L min^{-1} was directed to a fast condensation particle counter (Fast CPC; Model 3650, Kanomax Inc., Japan) for continuous monitoring of seed-particle number concentration, and the remaining 5 L min^{-1} was directed into the laminar flow reactor.

The performance and operational principles of the half-mini-DMA have been detailed previously (Liu et al., 2020). The instrument was first operated in scanning mode, gradually increasing the DMA voltage to obtain a full electrical mobility distribution of the polydisperse seed particles, and then switched to fixed mode by holding the voltage at the value corresponding to the electrical mobility of interest. DMA calibration was performed by electrospraying a methanol solution of tetraheptylammonium bromide and identifying the voltages associated with the peak transmission of the tetraheptylammonium cation monomer (THA^+) and dimer (THA_2^+), whose electrical mobilities at 298 K have been reported in previous studies(Carbone et al., 2016; Fang et al., 2014). A closed-loop sheath flow system was used, with the sheath flow rate fixed at 150 L min^{-1} to ensure high size resolution and minimize ion diffusion losses during classification. The sheath circuit was equipped with an in-line mass flowmeter (Model 4000, TSI Inc., USA) positioned upstream of the classification region. Under these conditions, the size resolution of the half-mini-DMA was approximately 30 for nanoparticles with a mobility diameter of 3.3 nm.

1.2 Inertness and charge stability of Ni-Cr oxide seed particles

Hot-wire generators operated with nichrome wires in clean dry air emit hydrophobic, non-soluble metal-oxide nanoparticles with well-defined sizes and minimal chemical contamination (Attoui, 2022; Fomenko et al., 2021; Picard et al., 2019). These Ni-Cr oxide nanoparticles contain essentially no native organic material and are non-volatile on the timescale and temperature range of our experiments. Under atmospheric pressure, their surfaces are rapidly passivated by an oxide shell, which strongly reduces their redox activity at room temperature (Attoui, 2022; Fomenko et al., 2021). Consequently, these seed nanoparticles behave largely as chemically inert condensation cores toward OOMs, so that the observed nanoparticle growth primarily reflects physical condensation onto an inorganic core rather than heterogeneous chemical transformation.

An additional consideration is the electrical charge carried by the 3–5 nm seed particles. Because they are mobility-selected by the half-mini-DMA, seed particles are predominantly singly charged, with multiply charged nanoparticles being negligible in this size range, consistent with bipolar charging theory (Kallinger and Szymanski, 2015). Downstream of the half-mini-DMA, the charged nanoparticles are transported through the flow reactor in a particle-free zero gas, without any additional ion source or strong electric fields. Classical ion–aerosol attachment theory shows that evolution of the charge distribution requires a reservoir of small ions for attachment and recombination (Hoppel and Frick, 1986). In the absence of such ions, the charge state is effectively frozen and remains unchanged within the 3-min residence time, implying that the singly-charged state of the 3–5 nm nanoparticles is stable along the flow reactor.

The TSI® 1-nm SMPS was operated at a sheath-to-aerosol flow ratio yielding a resolving power of 7 for nanoparticles with a mode diameter of 3.3 nm. As shown in Fig. S8, our half-mini-DMA setting yields a monodisperse distribution whose mode diameter is very close to the target, with geometric standard deviations (GSDs) typically $\leq$ 1.01, while peak number

concentrations ranged from (1.5–2.0) × 10^5 cm^{-3} for each size. By comparison, GSDs measured by the 1-nm SMPS were ~1.08 owing to its lower resolving power.

1.3 OOM generation in the PAM oxidation flow reactor

OOMs were produced via OH-initiated oxidation of toluene or ozonolysis of α-pinene in a Potential Aerosol Mass (PAM) oxidation flow reactor (OFR; Aerodyne Research Inc.) (Fig. S1). The flow into the PAM included dry and humidified zero air (15 L min^{-1}), VOC/N_2 mixture (15 sccm), and ozone (0.8 L min^{-1}), giving a total flow rate of ~16 L min^{-1} and a residence time of ~52 s.

For OH + toluene experiments, the PAM was operated under the OFR254 mode, in which OH radicals were generated in situ by 254-nm photolysis of ozone ($O_3 + h\nu \rightarrow O(^1D) + O_2$; $O(^1D) + H_2O \rightarrow 2\ OH$). Relative humidity was adjusted by a Nafion humidifier and monitored at the reactor outlet; all experiments were conducted at RH 44–53%. Toluene was supplied from a pressurized gas cylinder through a mass flow controller at 1–15 sccm. Ozone was generated externally and introduced at ~800 sccm. In selected experiments, NO was added to the PAM to produce controlled NOx levels. NOx and O_3 concentrations were measured by a NOx monitor (42i, Thermo Scientific Inc.) and an O_3 monitor (49i, Thermo Scientific Inc.), respectively. To terminate oxidation reactions downstream of the PAM and prevent OH-induced oxidation in the laminar flow reactor, 2.5 sccm of 10% carbon monoxide (CO) was added at the PAM outlet as an OH scavenger.

In parallel experiments, α-pinene was used as a precursor for ozonolysis-driven OOM formation under dark, OH-free conditions. The PAM functioned as a passive mixing and reaction zone, with ozone introduced upstream of the α-pinene flow; no UV irradiation or external OH generation was applied.

1.4 Main reaction zone and sampling configuration

Ni-Cr oxide seed nanoparticles were introduced into the laminar flow reactor through a glass conical injector, expanding from 1.9 cm to 20 cm in inner diameter with an opening angle of 9.4°. This geometry promotes a stable laminar flow and a parabolic velocity profile across the reactor cross-section. OOMs from the PAM were introduced through an annular inlet surrounding the particle flow axis; the ring-shaped geometry promotes rapid radial diffusion of OOMs and uniform mixing with the seed nanoparticles.

The main reaction zone extends 200 cm in length with a 20 cm inner diameter. At a total flow rate of 21 L min^{-1} (mean axial velocity U = 0.0111 m s^{-1}), this configuration yields a residence time of ~3 min, with Reynolds number $Re = \rho UD/\mu < 200$. Nine evenly spaced sampling ports are distributed along the axial direction: the first port is 35 cm downstream of the OOM injection plane, with the remaining ports at 20 cm intervals.

1.5 Online instrumentation

A nitrate chemical ionization mass spectrometer (nitrate-CIMS; Aerodyne Research Inc., USA, and Tofwerk AG, Switzerland) detected highly oxygenated organic molecules (HOM) in the gas phase. An iodide-ion-based chemical ionization mass spectrometer (iodide-CIMS; same manufacturers) provided complementary detection of moderately oxidized and semi-volatile compounds. A Vocus proton-transfer-reaction time-of-flight mass spectrometer (Vocus-PTR; same manufacturers) monitored VOC precursor consumption and quantified volatile and semi-volatile organics.

Particle measurements used a 1-nm DMA scanning mobility particle sizer (1-nm SMPS; Model 3938E57, TSI Inc., USA) covering 1–100 nm. During coagulation-only experiments, the 1-nm SMPS sampled sequentially at ports 1–9; during condensation experiments, it sampled at port 6 (residence time = 131 s). A particle size magnifier (PSM; Model A10, Airmodus Inc., Finland) and a nano-DMA scanning mobility particle sizer (nano-SMPS; Model 3936, TSI Inc., USA) sampled at the 180 s port to verify the absence of new-particle formation. A fast CPC (Model 3650, Kanomax Inc., Japan), placed downstream of the half-mini-DMA, monitored seed-particle number concentrations entering the flow tube.

S2. H_2SO_4, OOM measurements and quantification

Gaseous H_2SO_4 was detected by the nitrate-CIMS. Calibration was performed by introducing a known concentration of H_2SO_4 generated from OH-initiated oxidation of SO_2 under UV photolysis of water vapor, following the configuration described in ref.(Kürten et al., 2012). The resulting calibration coefficient was 8.03×10^9 cm^{-3}.

We define OOMs as molecules containing at least one C, H, and O atom. Three complementary mass spectrometric techniques were employed — Vocus-PTR, iodide-CIMS, and nitrate-CIMS — all equipped with long time-of-flight analyzers providing mass resolutions of 8,000–9,000 Th/Th. Because nitrate-CIMS provides more reliable quantification for HOM(Bianchi et al., 2019; Jokinen et al., 2012), whereas iodide-CIMS and Vocus-PTR yield semi-quantitative results based on reagent-ion binding affinities(Krechmer et al., 2018; Lopez-Hilfiker et al., 2016), we developed cross-instrument reconciliation rules (Section 3.4 below).

2.1 Vocus-PTR

Vocus-PTR was calibrated using a multi-component gas-phase standard mixture (Table S3) dynamically diluted to atmospherically relevant concentrations and introduced under the same conditions as for laboratory and ambient sampling. Background signals were determined by switching the inlet to zero air. For OOMs without gas-phase standards, sensitivities were estimated based on their proton-transfer reaction rate constants (k_i), using an empirical linear relationship derived from calibrated VOCs (Fig. S3) (Sekimoto et al., 2017). This approach assumes minimal fragmentation and efficient ion transmission, validated previously across a wide range of oxygenated organic compounds (Wang et al., 2020). To account for instrumental drift, the calibration was repeated hourly, with a correction factor F applied to ambient measurements based on inter-hour calibrant variability. OOM concentrations were calculated as

$$[\mathrm{OOM}_i] = \mathrm{C_{cal}} \times [\mathrm{OOM}_i \cdot \mathrm{H}^+] \times k_i \times \mathrm{F} \qquad \text{(S1)}$$

The systematic uncertainty is typically ±20% for directly calibrated compounds, but OOM concentrations may be overestimated by a factor of 2–10 owing to variations in ionization efficiencies and fragmentation patterns (Riva et al., 2019; Sekimoto et al., 2017).

2.2 Iodide-CIMS

Calibration of the iodide-CIMS followed the Lopez-Hilfiker et al. (2016) method (Lopez-Hilfiker et al., 2016). The same liquid-injection calibration system used for citric acid and PEG-7 was used to generate 11 gaseous calibrants (Table S4) at known mixing ratios under matched flow and temperature conditions. To account for transmission losses due to collisional declustering in the atmospheric pressure interface, we performed a declustering voltage scan to determine the stability of iodide–OOM adducts, which was achieved by incrementally increasing the electric field strength between the skimmer and the quadrupole entrance while keeping the ion transmission settings constant. Signal decay curves were fitted with a sigmoidal function to extract the voltage (dV_{50}) at which 50% of the signal was lost, which serves as a proxy for the binding enthalpy of each adduct. Adducts with high dV_{50} values (≥6 V) were considered strongly bounded and thus detectable with near-collision-limited sensitivity. For adducts with a weaker bound, the measured signal was corrected by a factor (S) derived from the extrapolated low-voltage transmission curve to account for ion losses during transmission. This correction enabled semi-quantitative sensitivity calibration for a wide range of OOMs, even in the absence of compound-specific calibration standards. Fig. S4 shows declustering-voltage scans of the iodide-CIMS for 11 calibrants of known concentrations (Table S4), from which we derive the empirical relationship between the measured dV_{50} and the instrument's normalized sensitivity. This calibration curve serves as a transfer function to estimate sensitivities for uncalibrated OOMs. For iodide-CIMS, sensitivities vary widely across functional groups, with uncertainties of 25%-50% for calibrated OOMs and 25%-80% for uncalibrated OOMs, resulting in an overall uncertainty of approximately 60% for a mixture of OOMs.

2.3 Nitrate-CIMS

We assume that all OOMs detected by the nitrate-CIMS exhibit the same ionization efficiency as H_2SO_4 and that the $OOM{\cdot}NO_3^-$ clusters are sufficiently stable to avoid dissociation during their residence within the mass spectrometer(Tröstl et al., 2016; Yao et al., 2018). Transmission efficiency (T) corrections for CIMS were performed following a method described in the literature(Heinritzi et al., 2016), i.e., a series of perfluorinated acids with varying molecular masses were introduced into nitrate-CIMS to derive an instrument-specific relative transmission curve. The concentration of each detected OOM was subsequently quantified using equation (S2), incorporating the corresponding relative transmission correction. The systematic uncertainty of the nitrate-CIMS measurement is +50%/−50%, coming from uncertainties in the calibration(Garmash et al., 2024; Stolzenburg et al., 2025).

$$[\mathrm{OOM_i}] = \mathrm{C_{H_2SO_4}} \times \frac{\mathrm{OOM_i} \cdot \mathrm{NO_3^-}}{\mathrm{NO_3^-} + \mathrm{HNO_3} \cdot \mathrm{NO_3^-} + (\mathrm{HNO_3})_2 \cdot \mathrm{NO_3^-}} \times \mathrm{T} \qquad (S2)$$

2.4 Cross-instrument reconciliation

Although the three instruments differ in their theoretical detection sensitivities, they detect overlapping sets of OOMs(Isaacman-VanWertz et al., 2017; Riva et al., 2019). Identical molecular formulas across instruments do not guarantee identical structures, given isomeric and structural diversity.

For OOMs detected by both iodide-CIMS and nitrate-CIMS (Fig. S5; n_o = 1–8, with strongest overlap at $n_o \approx 3$–6), the two estimates agreed within an order of magnitude only for species with n_o = 4–5, while diverging systematically at lower or higher oxygen numbers. Because CIMS sensitivity depends strongly on n_o, formulas with $n_o \leq 3$ were quantified by iodide-CIMS, those with $n_o \geq 6$ by nitrate-CIMS, and those with n_o = 4–5 were assigned the higher of the two estimates.

For OOMs detected by both Vocus-PTR and iodide-CIMS (Fig. S6), the two estimates showed larger discrepancies than for the iodide–nitrate pair, reflecting fragmentation of multifunctional OOMs in Vocus-PTR (Li et al., 2022; Zhang et al., 2025). Following the same logic, formulas with n_o = 0 or 1 were quantified by Vocus-PTR, those with $n_o \geq 4$ by iodide-CIMS, and those with n_o = 2 or 3 were assigned the higher of the two estimates.

For OOMs detected by both Vocus-PTR and nitrate-CIMS, the nitrate-CIMS estimate was used. For species detected by all three instruments, the iodide-CIMS / nitrate-CIMS rule was applied and the Vocus-PTR estimate was discarded.

2.5 Real-time axial concentration profiles in the flow reactor

In OOM mixture-driven growth experiments. We characterized OOMs' concentrations along the axial direction for both toluene + OH and α-pinene + O_3 experiments. OOMs were sampled at nine ports under identical inlet and ion-source settings. For each detected OOMs, the measured concentrations at nine sampling ports (C_t) were compared with the concentration at the 9th ports with a residence time of 180 s (C_{180s}), and the obtained $\ln(C_t/C_{180s})$ was regressed against the residence time to derive the concentration trend of each detected OOMs (Fig. S7).Then, the time-dependent concentration profile of each OOM was used as an input to the OOM concentration term of particle-growth model to derive the modelled growth rate, thereby minimizing simulation biases arising from OOM concentration gradients along the flow tube.

S3. Volatility parameterization of OOMs

Because direct volatility measurements of gas-phase OOMs are not feasible, their saturation concentrations C* are conventionally estimated from molecular formulas as a function of carbon (n_C), oxygen (n_O), and nitrogen (n_N) atom counts (Donahue et al., 2011):

$$\log_{10}C^*(300\mathrm{K}) = (25 - n_C)b_C - (n_O - 3n_N)b_O - 2\frac{(n_O - 3n_N)n_C}{(n_C + n_O - 3n_N)}b_{CO} - n_N b_N \qquad (S3)$$

where b_C=0.493, b_O=1.392, b_{CO}=-0.532, and b_N=2.402 from (Zhang et al., 2026). OOM volatility at ambient temperature was obtained by correcting for the temperature effect:

$$\log_{10}C^*(T) = \log_{10}C^*(300K) + \frac{\Delta H_{vap}}{R\ln(10)}\left(\frac{1}{300} - \frac{1}{T}\right) \quad (S4)$$

in which, the evaporation enthalpy ΔH_{vap} is obtained with following equation:

$$\Delta H_{vap}[kj\ mol^{-1}] = -5.7 \cdot \log_{10}C^*(300K) + 129 \quad (S5)$$

S4. Calculation of simulated growth rates

Following (Stolzenburg et al., (2022), nanoparticle growth was modeled using a monodisperse organic-growth framework that solves the coupled ordinary differential equations governing condensational mass transfer across VBS bins. Sulfuric acid condensation is also incorporated and is assumed to be kinetically limited:

$$\frac{dC_{i,p}}{dt} = N_p\beta_{i,p}[C_i^v - a_{i,p}C_i^0] \quad (S6)$$

$$\frac{dC_{sa,p}}{dt} = N_p\beta_{sa,p}C_{sa}^v \quad (S7)$$

where $C_{i,p}$ is the mass concentration of the i^{th} OOM in the particle phase, C_i^v is the mass concentration of the i^{th} OOM in the gas phase, and C_i^0 is the saturation mass concentration of the i^{th} OOMs at the temperature of the experiment. N_p is the monodisperse particle population number concentration, and, in this framework, does not influence the resulting GR of the model. $\beta_{i,p}$ is the collision rate coefficient for collision of the i^{th} OOM with the growing particle population, which is assumed to follow a hard-sphere collision kernel based on bulk density and spherical assumptions

Particle phase activity $a_{i,p}$ is calculated as $a_{i,p} = X_{i,p}\gamma_{i,p}K_{i,p}$, where $X_{i,p} = c_{i,p}^s/c_p^s$ is the mass fraction of the i^{th} OOM in particle phase, $c_{i,p}^s$ is the mass of the i^{th} OOM in particle phase, and c_p^s is the sum of $c_{i,p}^s$ in particle phase; $\gamma_{i,p}$ is the mass based activity coefficient in the gas-phase organics, and is assumed to be 1; $K_{i,p}$ is the Kelvin coefficient, and is calculated as $K_{i,p} = \exp(\frac{4\sigma_{i,v}M_{i,v}}{RT\rho_{i,v}dp})$, which in turn accounts for the increased equilibrium vapor pressure over curved surfaces and can be estimated using (bulk) organic surface tension $\sigma_{i,v}$, density $\rho_{i,v}$, and the molecular mass $M_{i,v}$ of the condensing vapors.

S5. Field measurements at Lake Tai

A field campaign was conducted from 4th July to 20th September, 2023 in the National Field Observation and Research Station for the Lake Ecosystem of Lake Tai (31°42′N, 120°22′E, ~5 m above sea level), located in a suburban area of Jiangsu Province, China. The site is influenced by both anthropogenic emissions from surrounding industrial and residential regions and natural emissions from nearby freshwater lake systems.

PNSDs were measured using a TSI® 1-nm SMPS, a TSI® Long-SMPS, and an Airmodus® PSM, together covering a size range from 1.2 to 700.0 nm. These three instruments operated in parallel with time resolutions of 1-4 min, and were used to derive particle GRs across the full nucleation-to-accumulation mode range. Twelve NPF events were observed during the field measurements, among which four events were selected for more detailed analysis. These four events featured moderate background condensation sinks and relatively smooth growth behavior, which favors GR estimation, because these conditions minimized interference from coagulation and permitted a robust comparison of field measurements with modeled monodisperse growth driven by condensation of organic vapors.

To quantify ambient OOMs at Lake Tai, we deployed the same suite of instruments and the same settings as in the laboratory: a nitrate–CIMS, an iodide–CIMS, and a Vocus-PTR. For nitrate-CIMS, sampling was through a 0.8 m and 3/4-inch inner diameter (ID) stainless-steel tube, and the sample flow rate was 10 L min^{-1} (more details in our previous study(Yao et al.,

2018)). For iodide-CIMS, a 0.8 m polytetrafluoroethylene (PTFE) tubing (0.38-inch ID, 0.50-inch OD) was used with a bypass blower to maintain a total sample flow of 15 L min^{-1}, of which 2 L min^{-1} was drawn into the iodide-CIMS. For the Vocus-PTR, a 0.8 m PTFE tubing (0.12-inch ID, 0.25-inch OD) was used with a bypass blower to maintain a total sample flow of 5 L min^{-1}, of which 0.08 L min^{-1} was drawn into the Vocus-PTR.

S6. Generation and quantification of citric acid and PEG-7 vapors

Citric acid or PEG-7 vapors were generated by immersing an evaporator of pure compound in a hot water bath and delivering the headspace gas to the flow reactor. Different concentration levels were produced by adjusting the bath temperature: 45–80 °C for citric acid (restricted to avoid potential thermal decomposition above ~120 °C; Fig. S21) and 52–85 °C for PEG-7.

Citric acid was quantified with the nitrate-CIMS, and PEG-7 with the iodide-CIMS. Instrument sensitivities were determined by liquid-injection calibration: the citric acid or PEG-7 solution was delivered to a liquid nebulizer (TR-30-A1, Meinhard Inc., USA) at 0.1–0.2 mL h^{-1}, together with a dilution gas (zero air) flow of 1 L min^{-1}, using a gas-tight syringe (1002LT, Hamilton Inc., Switzerland) driven by a syringe pump (Fusion 200-x, Chemyx Inc., USA). The nebulizer outflow was further mixed with another zero-air flow at 1 L min^{-1} in a 200 mL glass mixing flask to allow full evaporation of the droplets. The calibration stream was then diluted with a third zero-air flow to match instrument demands (10 L min^{-1} for nitrate-CIMS; 2 L min^{-1} for iodide-CIMS), with transfer lines kept < 10 cm to minimize losses. No liquid condensation was visible on the flask walls. Linear responses were obtained, yielding calibration factors of 1.35×10^{12} cm^{-3} for citric acid and 9.44×10^{11} cm^{-1} for PEG-7 (Fig. S2).

Text S7. Box model for heterogeneous reactions' contribution to growth of 3-15 nm particles

The Community Multiscale Air Quality (CMAQ) model is a widely used tool for atmospheric chemistry. Its heterogeneous chemistry module simulates how gases, such as nitrogen oxides, isoprene oxidation products, and carbonyl compounds, react on aerosol particles' surface to form particulate compounds. In this section, we adapt this module to investigate how heterogeneous reactions drive the growth of 3 - 10 nm nanoparticles, thereby contributing to the growth of newly formed particles at the Lake Tai campaign in China.

The original CMAQ model includes 54 reaction pathways, covering nitrogen oxides, isoprene-derived compounds, carbonyls, halogen compounds, and primary organic carbon. These reactions occur across three particle size ranges: nucleation mode (< 0.1 μm), accumulation mode (0.1 - 1 μm), and coarse mode (> 1 μm). The module calculates reaction rates based on gas concentrations, particle surface areas, and uptake efficiencies to estimate aerosol growth. However, the complexity and reliance on multiple inputs of the module make it challenging to study heterogeneous reactions over small particles in the 3 - 15 nm range.

We simplified the CMAQ module into a box model tailored for 3 - 15 nm particles, which belong to the nucleation mode. The full set of 54 reactions was reduced to 21 by excluding pathways irrelevant to our study, including that (1) we consolidated multiple isoprene-derived epoxydiols (IEPOX) and methacrylic acid epoxide (IMAE) reactions into a single pathway; (2) halogen reactions, which are significant in coastal areas but not at the Lake Tai area, were omitted due to their limited relevance and lack of local data; and (3) reactions associated with primary organic carbon in the particles were excluded. Heterogeneous oxidation of organic carbon mainly affects the surface aging of pre-existing larger particles, and its contribution to the early growth of nucleated 3-15 nm particles is negligible. The retained pathways focus on key species like N_2O_5, NO_2, HNO_3, IEPOX, IMAE, $NO_3\cdot$, glyoxal (GLY), methylglyoxal (MGLY), and organic nitrates.

The box model emphasizes on reactions occurring on 3 - 15 nm particles, ignoring larger particles. Heterogeneous reaction rate constant (k_{gas}), which describes the rate at which gaseous species react on particle surfaces (s^{-1}), is calculated using the general formula:

$$k_{gas} = \frac{\gamma \cdot A \cdot \bar{c}}{4} \quad \text{(S8)}$$

where γ is the uptake coefficient, A is the particle surface area per unit volume ($m^2\ m^{-3}$), and $\bar{c}$ is the mean molecular speed of the gas species ($m\ s^{-1}$) that is derived as:

$$\bar{c} = \sqrt{\frac{8RT}{\pi M}} \quad \text{(S9)}$$

where R is the universal gas constant (8.314 $J\ mol^{-1}\ K^{-1}$), T is the absolute temperature (K), and M is the molar mass of the gas species ($kg\ mol^{-1}$).

For IEPOX and IMAE that significantly contribute to SOA formation, γ is dynamically calculated based on Hanson et al. (1994)(Hanson et al., 1994) and Pye et al. (2013)(Pye et al., 2013):

$$\gamma = \frac{1}{\alpha^{-1} + \frac{v \cdot r}{4HRT D_l (q/\tanh(q) - 1)}} \quad \text{(S10)}$$

where α^{-1} is the inverse of the mass accommodation coefficient, v is mean molecular speed ($m\ s^{-1}$), r is the particle radius (m), H is Henry's law constant ($mol\ L^{-1}\ atm^{-1}$), D_l is the bulk diffusion coefficient within the particle ($m^2\ s^{-1}$), and q is a dimensionless reaction-diffusion parameter, defined as $q = r\sqrt{\frac{k_{particle}}{D_l}}$, with $k_{particle}$ defined as a particle-phase reaction rate constant (s^{-1}).

Temperature, humidity, NO_2, IEPOX, and IMAE concentrations were sourced from the Lake Tai field measurements; N_2O_5, HNO_3, GLY, and MGLY (Table S5) were obtained from WRF-CMAQ model simulation (Supplementary Text 2), and $NO_3\cdot$ is set with a common parameter, 5×10^8 cm^{-3}. Environmental conditions used in the model simulation represent typical urban conditions and are comparable to those used in previous studies (Table S6)(Shi et al., 2019; Song et al., 2019; Zheng et al., 2015).

The model runs a period of over 12,000 s, tracking how heterogeneous reactions contribute to particle mass and size growth. The mass increase per time step is calculated based on the reaction rate and gas-phase concentration:

$$\Delta m = k_{gas} \cdot C \cdot n_{air} \cdot 10^{-6} \cdot M \cdot \Delta t \quad \text{(S11)}$$

where Δm is the mass contribution ($g\ m^{-3}$), C is the gas-phase concentration (ppm), n_{air} is the air molecule density ($mol\ m^{-3}$), M is the molecular weight ($g\ mol^{-1}$), and Δt = 60 s is the time step. This mass is then used to update the particle volume and diameter. The new particle volume is determined as:

$$V_{new} = V_{initial} + \frac{\Delta m/N}{\rho} \quad \text{(S12)}$$

where $V_{initial}$ is the initial volume of a single particle (m^3), N is the particle number density (m^{-3}), and ρ is the particle density ($g\ m^{-3}$). The new diameter is calculated as:

$$d = 2 \cdot \left(\frac{3V_{new}}{4\pi}\right)^{1/3} \quad \text{(S13)}$$

Finally, the contribution ratio for each reaction is computed as:

$$Ratio_i(\%) = \frac{m_i}{\sum m_i} \cdot 100 \quad \text{(S14)}$$

This box model quantifies how heterogeneous reactions of gas-phase species contribute to the mass of 3-15 nm particles, particularly those of IEPOX/IMAE, nitrogen oxides, and GLY/MGLY. By reducing computational demands, it enables an efficient analysis with limited field data.

S8. Configuration of WRF-CMAQ

To fully quantify the effects of heterogeneous reactions on particle size growth, key species including N_2O_5, HNO_3, organic nitrates, GLY, and MGLY were obtained from simulations using a regional three-dimensional chemistry transport model, WRF-CMAQ (Weather Research and Forecasting - Community Multiscale Air Quality Modeling System).

Domains and configurations of the current WRF modelling (https://www.mmm.ucar.edu/models/wrf) are identical to those in a previous study(An et al., 2022). A version 5.5 CMAQ (https://github.com/USEPA/CMAQ) was employed with the Community Regional Atmospheric Chemistry Multiphase Mechanism (CRACMM). Inorganic aerosol thermodynamic equilibrium was simulated using ISORROPIA(Fountoukis and Nenes, 2007). Anthropogenic emissions in the Yangtze River Delta region for 2021 were updated(An et al., 2021), while emissions in other regions were derived from the Model Inter-Comparison Study (MIX) emission inventory for 2010, the Multiresolution Emission Inventory for China (MEIC-2019, http://meicmodel.org), and the Shipping Emission Inventory Model(Liu et al., 2019). In addition, emissions of intermediate and semi-volatile organic compounds (I/SVOCs) were incorporated into the model(An et al., 2022). Biogenic VOC emissions were estimated using the Model of Emissions of Gases and Aerosols from Nature (MEGAN v2.1)(Guenther et al., 2006). Both anthropogenic and biogenic VOCs were speciated into CRACMM-compatible species using the SPECIATE input and biogenic species mappings (https://github.com/USEPA/CRACMM/tree/main/emissions) using the Sparse Matrix Operator Kernel Emissions (SMOKE, https://cmascenter.org/smoke) model.

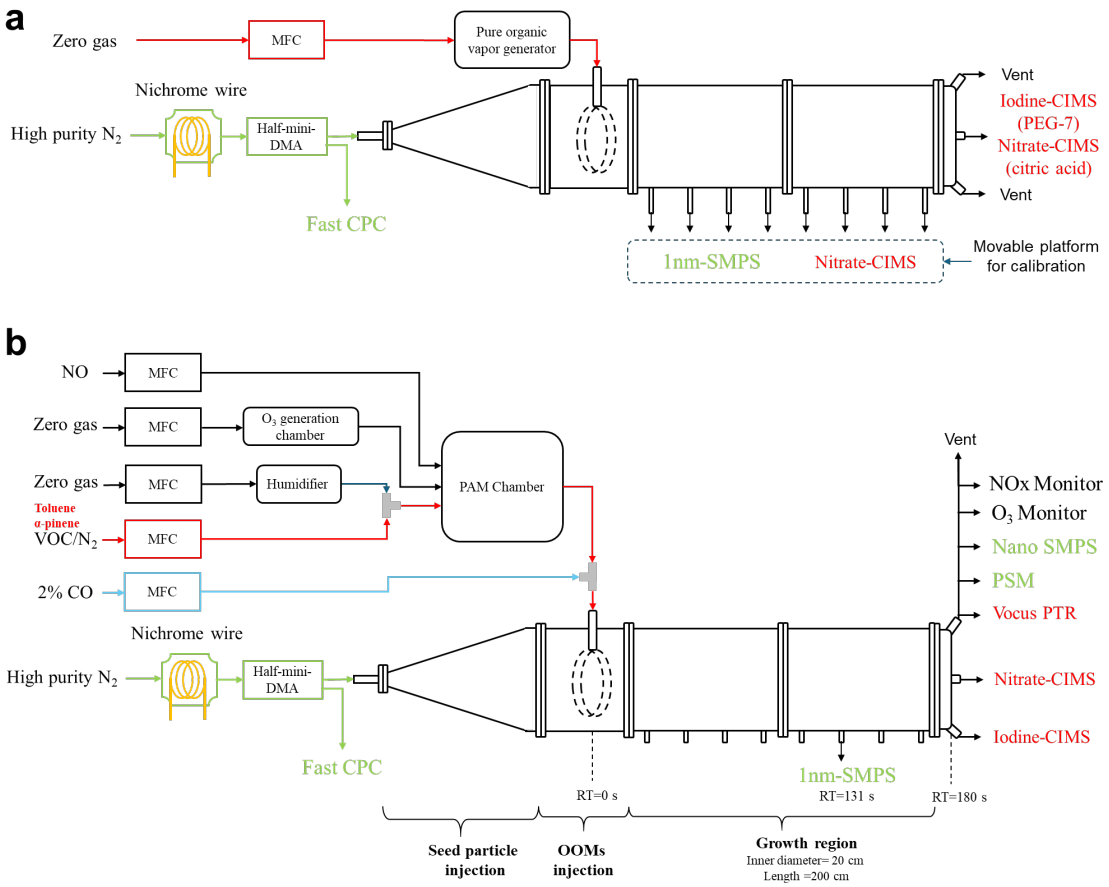


Fig. S1. Schematics of the experimental setup. a, Experimental setup for coagulation growth and condensational growth of nanoparticles by a single OOM. Particle and vapor-phase measurements are performed using a suite of instruments: Fast CPC and 1 nm-SMPS for PNSD detection; Iodide-CIMS (PEG-7), and nitrate-CIMS (citric acid) for gaseous organics' detection. SMPS and CIMS are mounted on a movable platform, allowing sampling of particles and vapors at different axial positions along the flow reactor. **b**, Experimental setup for condensational growth of nanoparticles by an OOM mixture. Toluene or α-pinene, as VOC precursors, is introduced into the PAM where OOMs are produced with water vapor being added through a humidifier. The PAM outflow with OOMs is then directed into the laminar flow reactor, where particle growth occurs. Particle and vapor-phase measurements are performed using a suite of instruments: Fast CPC, PSM, Nano-SMPS, and 1-nm SMPS for PNSD detection; and Vocus-PTR, iodide-CIMS, and nitrate-CIMS for gaseous OOMs' detection.

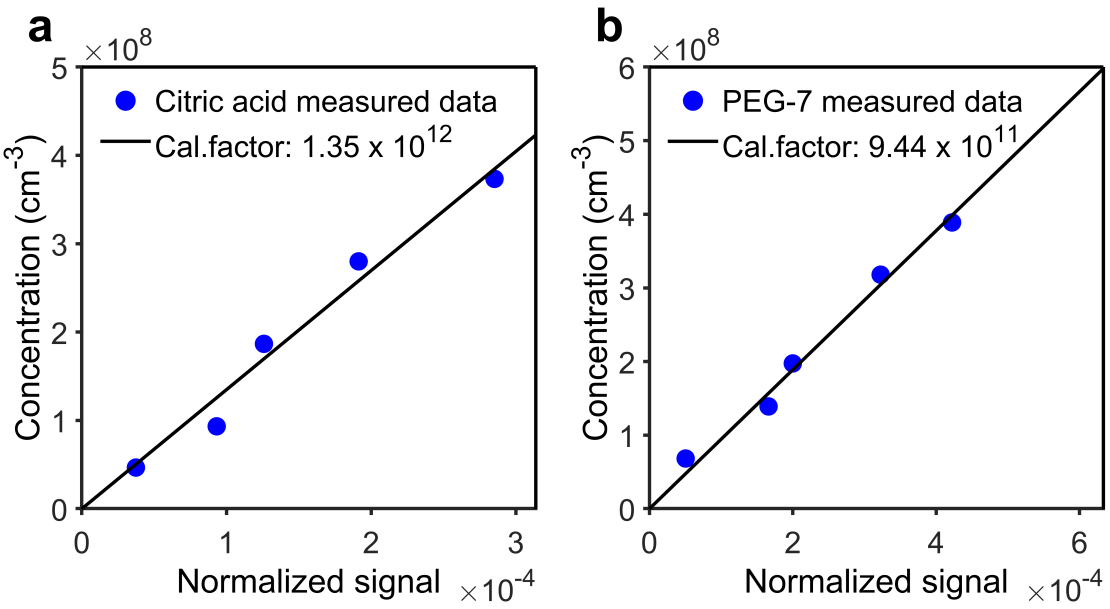


Fig. S2. Calibration of (a) citric acid by nitrate-CIMS and (b) PEG-7 by iodide-CIMS. The y-axis shows the calibrated concentration (cm^{-3}) obtained from a liquid-injection calibration system, and the x-axis shows the normalized signal, defined as the analyte ion signal divided by the corresponding reagent ion signal. Blue circles denote measurements, and black lines indicate the linear fits, whose slopes give the calibration factors.

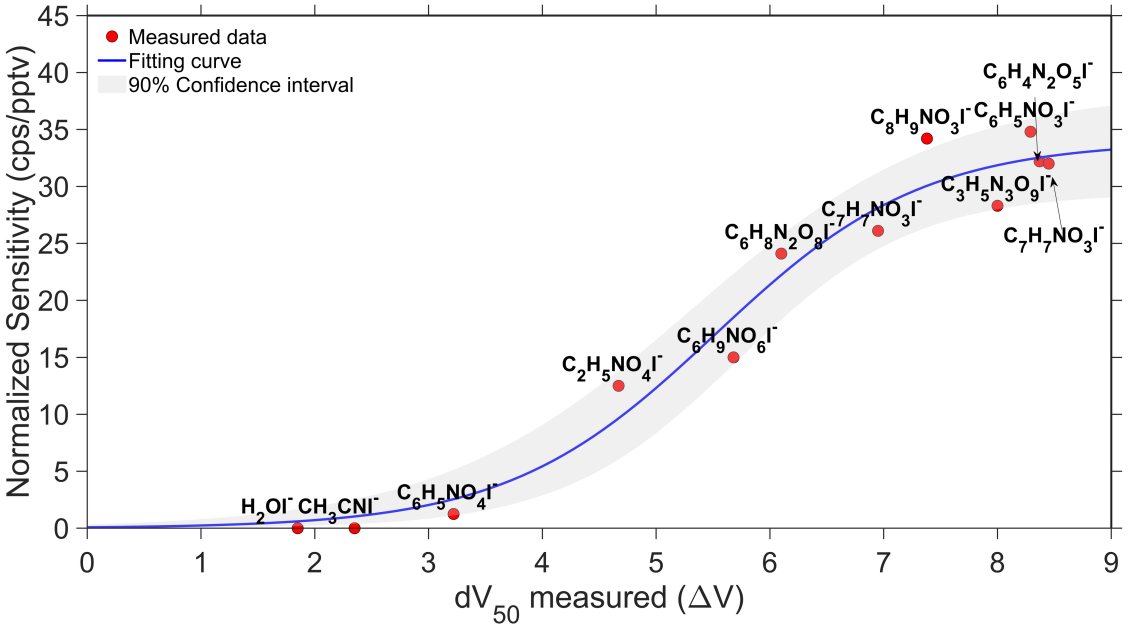


Fig. S3. Relationship between declustering voltage (dV_{50}) and sensitivity for detection of I^- adducts in iodine-CIMS. The plot shows the dependence of normalized instrument sensitivities (cps $pptv^{-1}$) on the measured declustering voltages (dV_{50}) for various I^- adducts detected by iodine-CIMS. Red circles represent measurements, the blue line denotes the fitted curve, and the shaded grey area indicates the 90% confidence intervals.

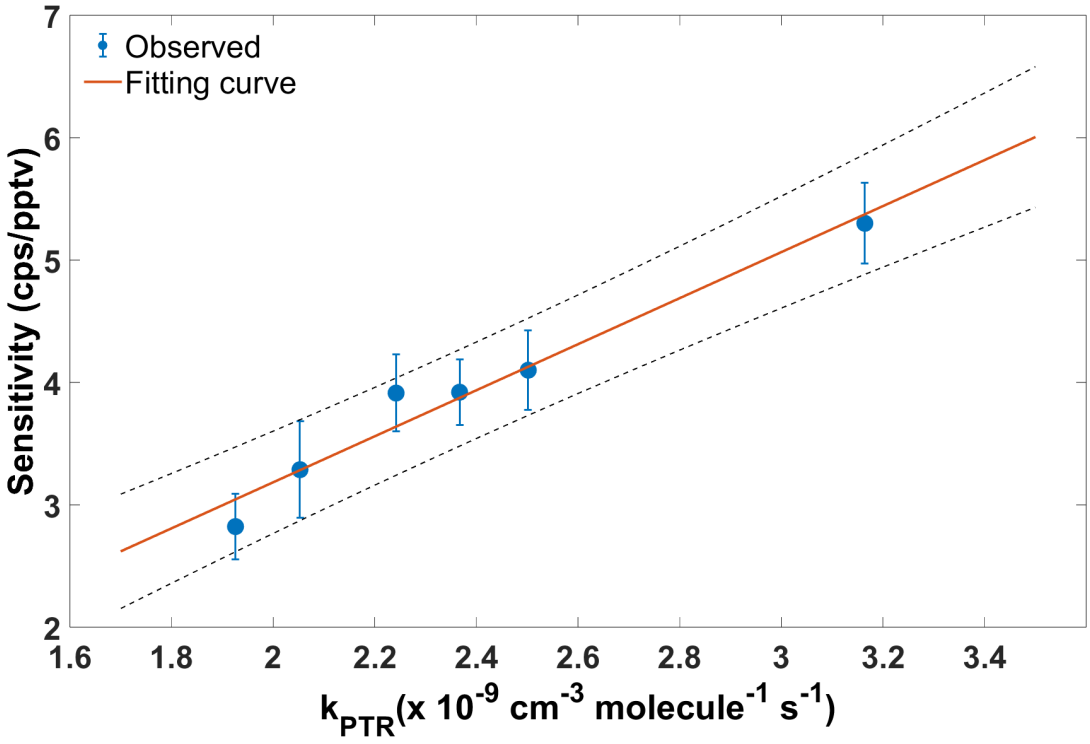


Fig. S4. Correlation between sensitivities and proton-transfer reaction rate constants in Vocus-PTR. The dashed lines denote 95% confidence intervals.

315

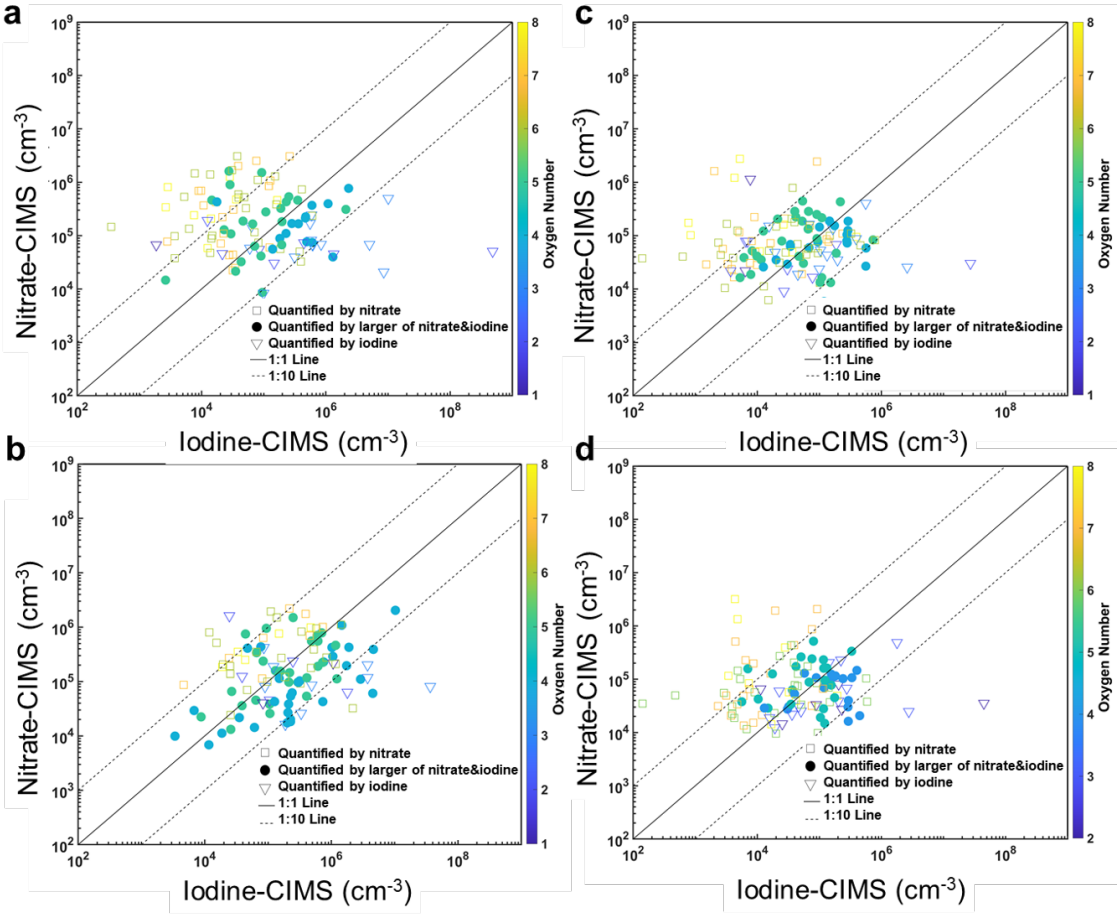


Fig. S5. Intercomparison of concentrations of OOMs detected by both nitrate-CIMS and iodine-CIMS in the flow reactor experiments. a, Toluene + OH (NOx < 1 ppb), **b,** Toluene + OH (NOx = 44 ppb), **c,** α-pinene + O_3 (NOx < 1 ppb), and **d,** α-pinene + O_3 (NOx = 44 ppb). Squares represent OOMs' concentrations quantified by nitrate-CIMS (oxygen number ≥ 6), triangles represent those quantified by iodine-CIMS (oxygen number ≤ 3), and circles indicate the larger of the two quantifications. The color of the data points denotes the oxygen number of OOMs. The solid line indicates the 1:1 ratio, while the dashed lines represent 1:10 or 10:1 ratio.

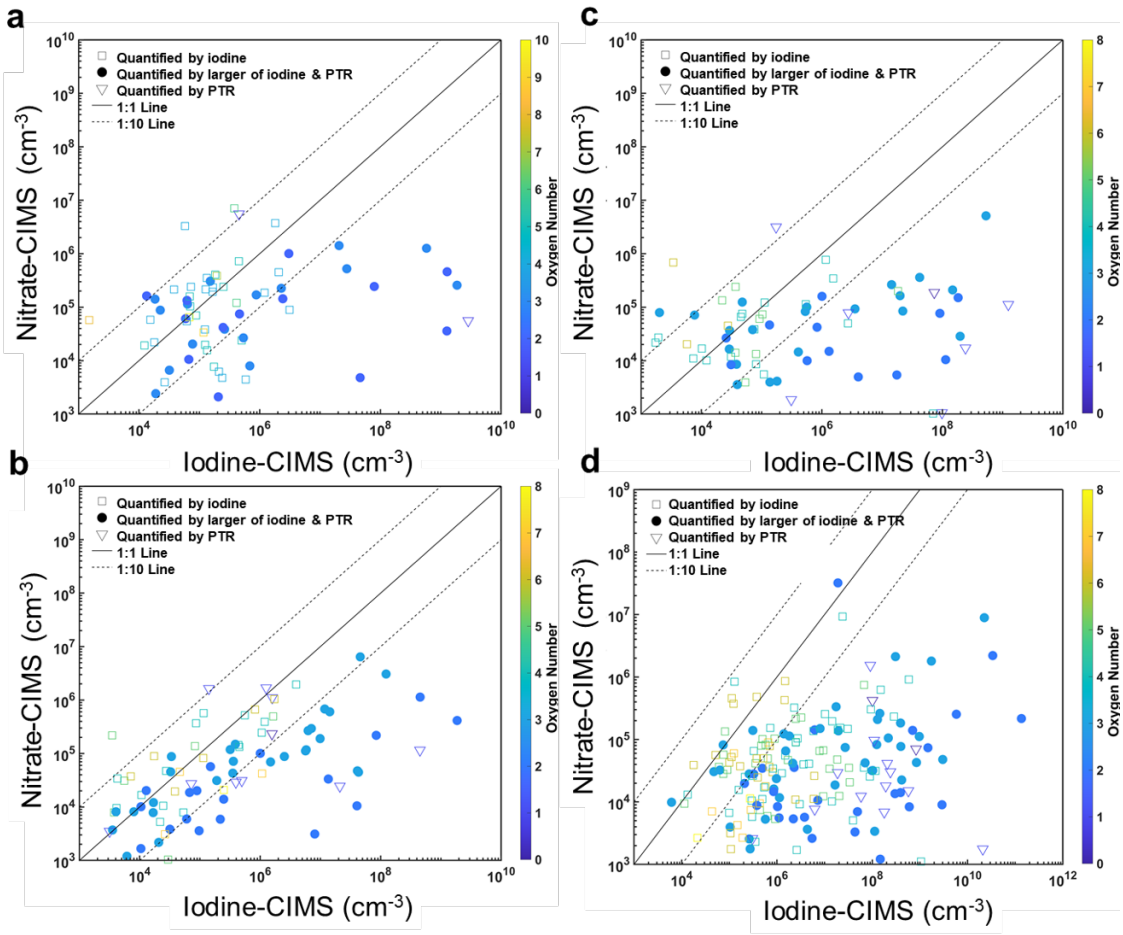


Fig. S6. Intercomparison of concentrations of OOMs detected by both iodine-CIMS and Vocus-PTR in the flow reactor experiments. a, Toluene + OH (NOx < 1 ppb), **b,** Toluene + OH (NOx = 44 ppb), **c,** α-pinene + O_3 (NOx < 1 ppb), and **d,** α-pinene + O_3 (NOx = 44 ppb). Squares represent OOMs' concentrations quantified by iodine-CIMS (oxygen number ≥ 4), triangles represent those quantified by Vocus-PTR (oxygen number ≤ 1), and circles indicate the larger of the two quantifications. The color of the data points denotes the oxygen number of OOMs. The solid line indicates the 1:1 ratio, while the dashed lines represent 1:10 or 10:1 ratio.

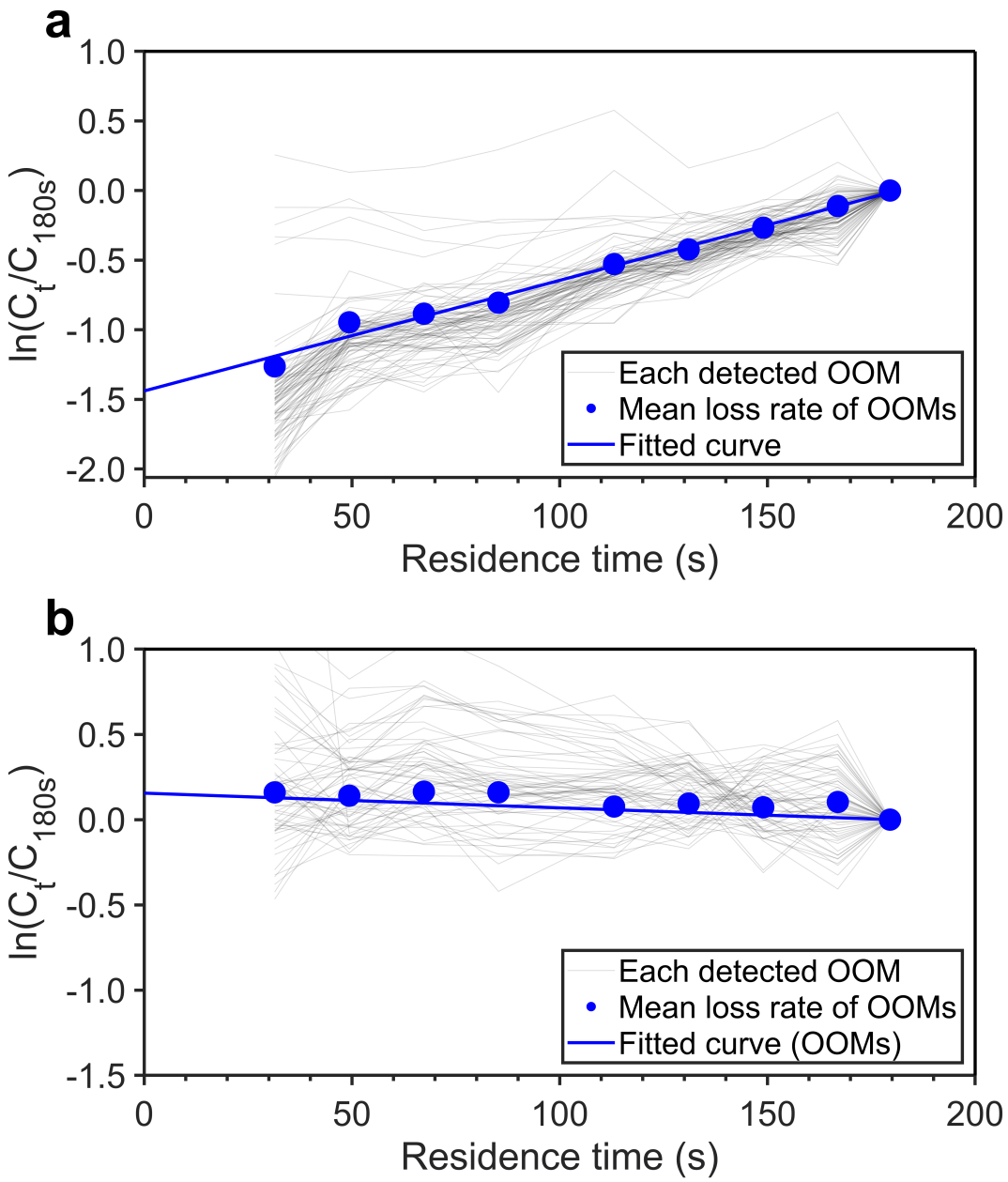


Fig. S7. Real-time concentrations of OOMs in the laminar flow reactor. a, α-Pinene + O_3 experiments. **b**, Toluene + OH experiments. The grey lines show ln (C_t/C_{180s}) for individual detected OOMs, where C_t is the measured concentration at each of the nine axial sampling ports and C_{180s} is the concentration at the last port (residence time = 180 s). Blue points denote the mean of OOMs at each sampling port and the blue line represent the linear fit.

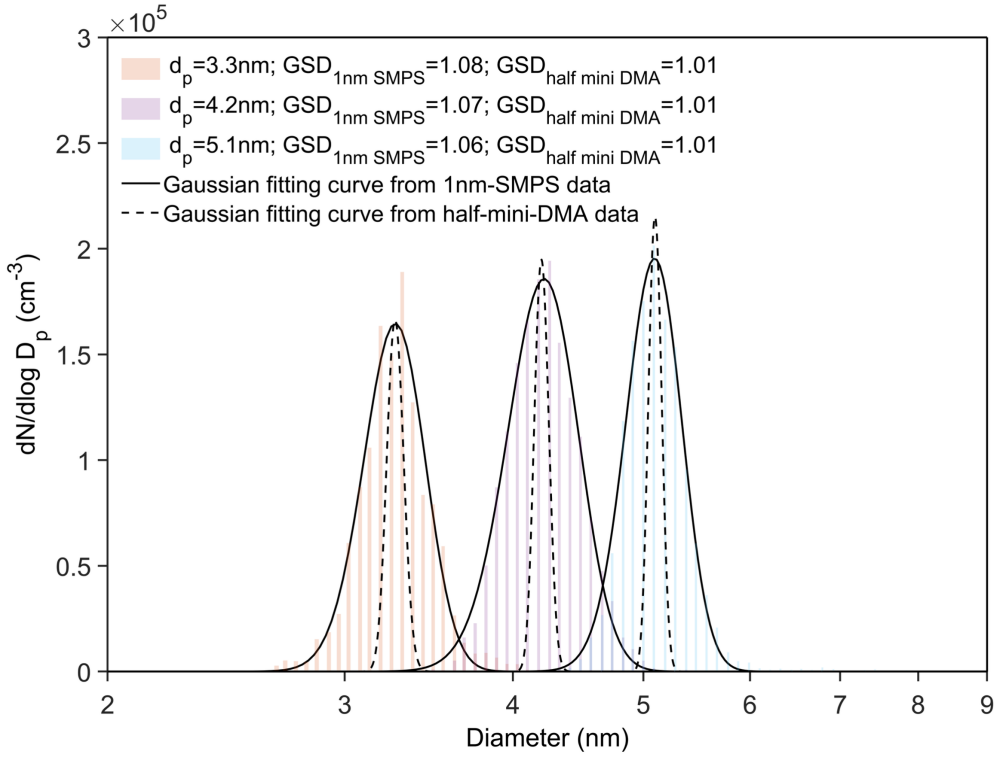


Fig. S8. PNSDs of monodisperse Ni-Cr oxide seed particles in the laminar flow reactor measured by the 1-nm SMPS and the half-mini-DMA, respectively. Colored bars show the PNSD measured by the 1-nm SMPS used to derive the particle mode diameters (D_p) and geometric standard deviations ($GSD_{1\text{-nm SMPS}}$), and black solid lines indicate the gaussian fitting curves. The dashed black lines indicate gaussian fitting curves of seed particles' PNSD measured by the half-mini-DMA. The fitted mode peaks at 3.3 nm, 4.2 nm, and 5.1 nm demonstrate that each size setting yields a single, narrow mode close to the target diameter.

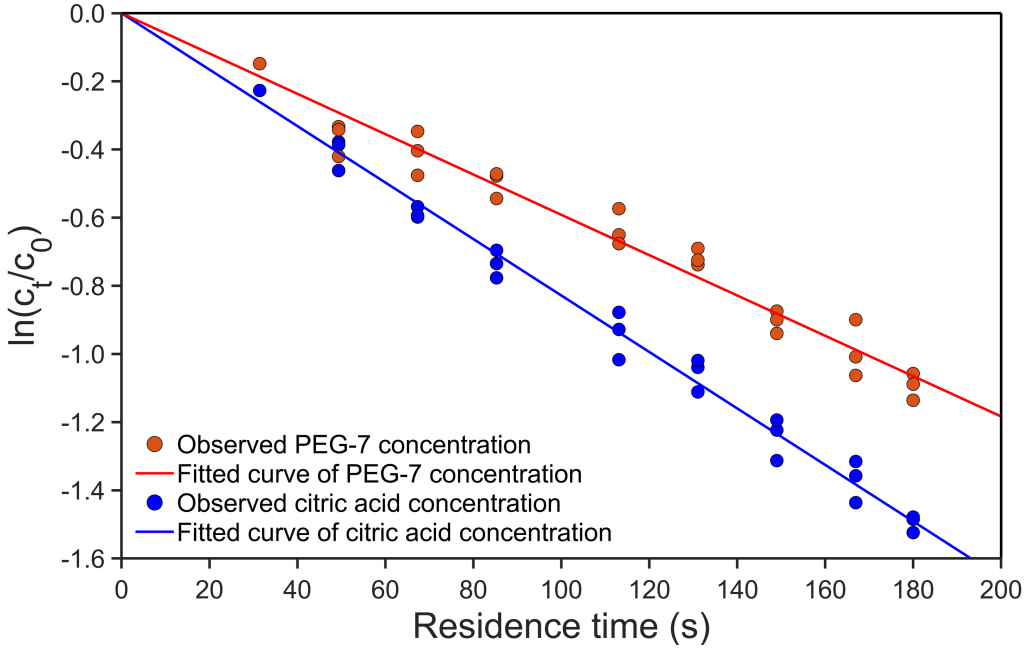
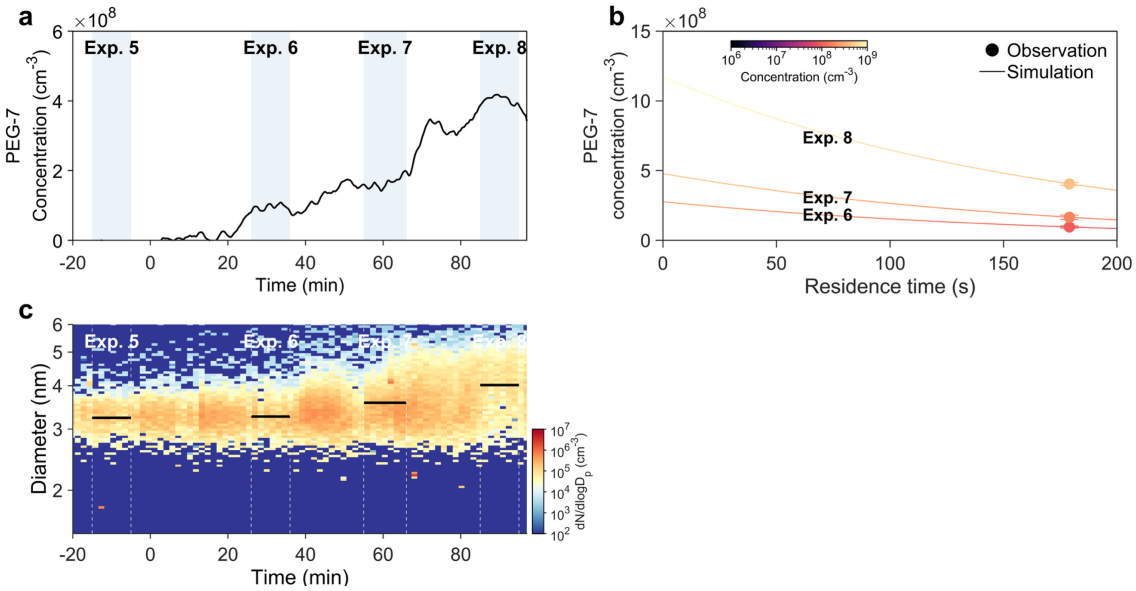


Fig. S9. Wall loss of citric acid and PEG-7 in the particle growth region of the flow reactor. Natural logarithm of the normalized citric acid and PEG-7 concentration (ln (C_t/C_0)) as a function of residence time is plotted. The data points correspond to the citric acid or PEG-7 concentrations observed at the 9 axial sampling points along the flow reactor. The line represents the exponential fit with the pseudo-first-order loss rate constant, yielding $k_{loss-citric\ acid}$ = 0.0083 s^{-1} and $k_{loss-PEG7}$ = 0.0059 s^{-1}.



355 **Fig. S10. Growth of monodisperse Ni-Cr oxide particles driven by condensation of PEG-7 in the laminar flow reactor.** **a,** Profiles of PEG-7 concentrations measured by iodine-CIMS at a fixed residence time of 180 s in the laminar flow reactor; shaded intervals denote Exp. 5–8, among which PEG-7 exposure was zero in Exp. 5. **b,** Observed PEG-7 concentrations at a residence time of 180 s for Exp. 6-8. Colored lines represent back-calculated concentrations of PEG-7 with incorporation of wall loss corrections using the loss-rate coefficient of PEG-7. **c,** PNSDs of Ni-Cr oxide particles during Exp. 5–8. Vertical
360 dashed white lines mark experimental boundaries, and horizontal black lines indicate the mean mode particle diameter in each experiment.

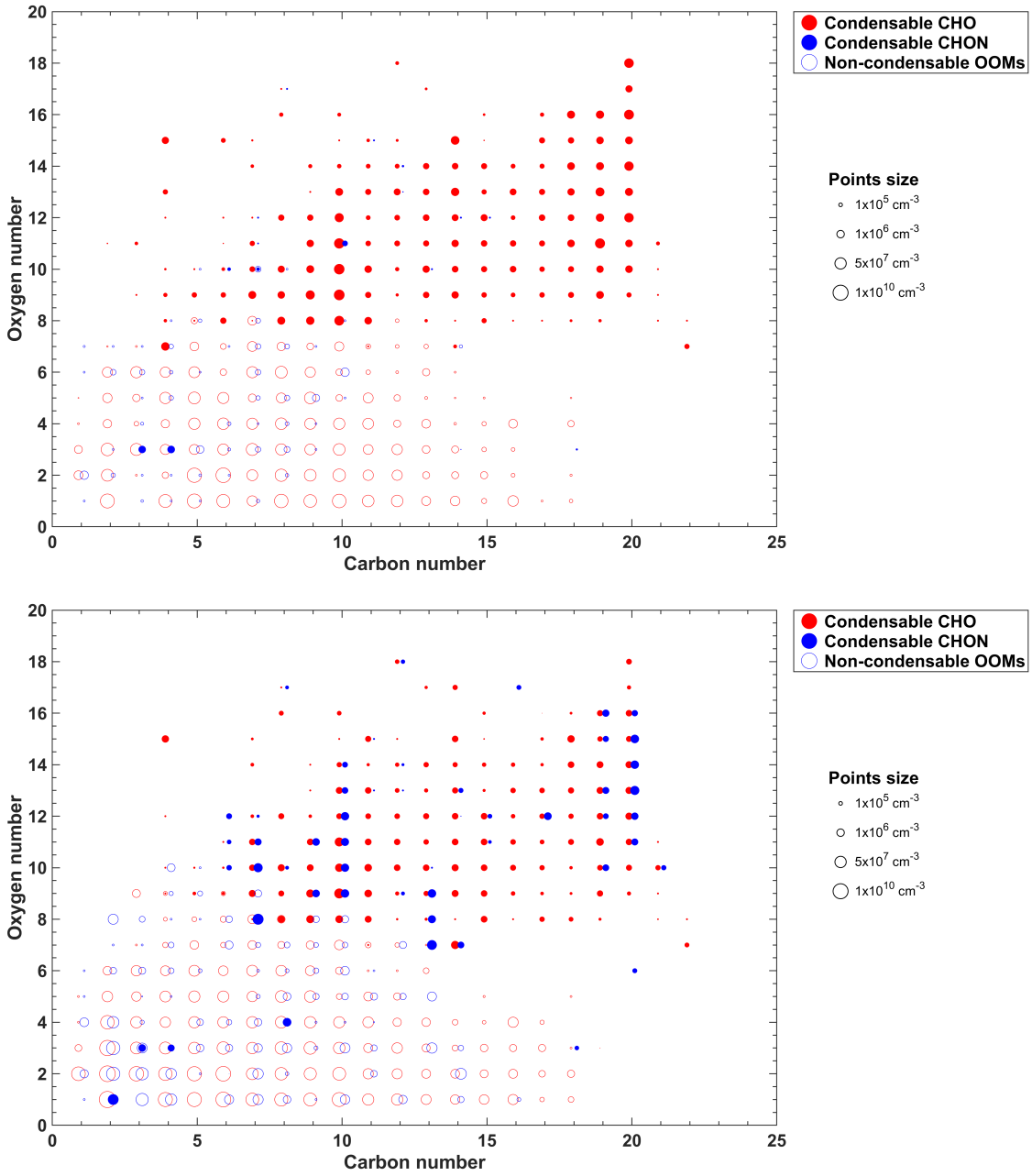


Fig. S11. Distributions of oxygen number and carbon number for OOMs formed in α-pinene + O_3 + NOx (< 1 ppb) (upper panel, corresponding to Exp. 12) and α-pinene + O_3 + NOx (44 ppb) (lower panel, corresponding to Exp. 16,) experiments, respectively. Red circles represent condensable CHO compounds for 3.3 nm particles, blue circles represent condensable CHON compounds, and hollow circles represent non-condensable OOMs due to Kelvin effect.

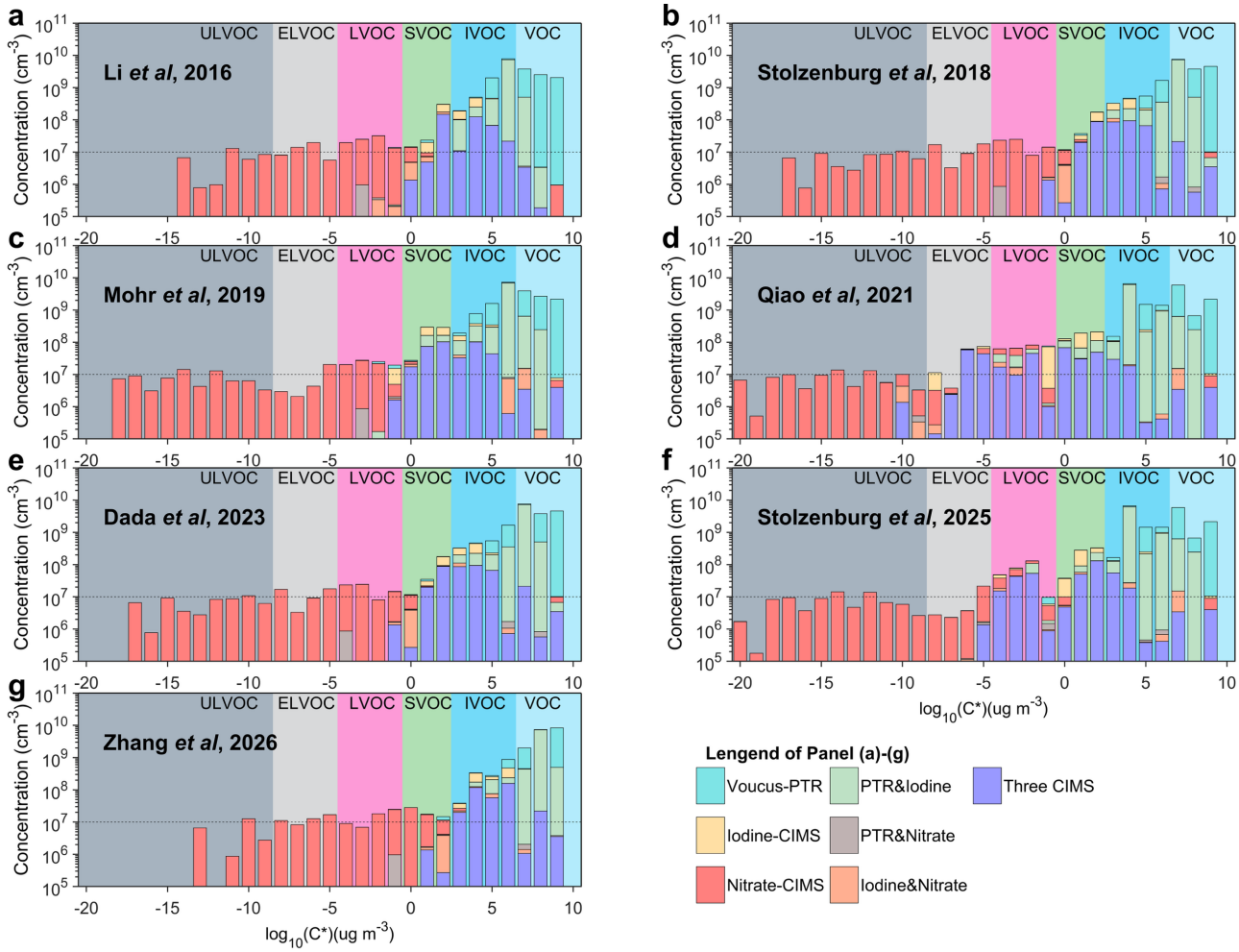


Fig. S12. Comparison of OOM volatility distributions derived from seven volatility parametrizations for α-pinene + O_3 under low NOx conditions (NOx < 1 ppb) (Exp. 12). Panels (**a-g**) show the effective saturation concentration ($\log_{10}C^*$) distributions of OOMs, calculated using seven volatility parametrizations ((Li et al., 2016); (Stolzenburg et al., 2018); (Mohr et al., 2019); (Qiao et al., 2021); (Dada et al., 2023); (Stolzenburg et al., 2025); and (Zhang et al., 2026), respectively). The colored background regions indicate volatility classes ranging from ULVOC to VOC. Stacked bars represent the concentrations of OOMs detected by at least one of the three CIMS. Please refer to the main text for quantification rules.

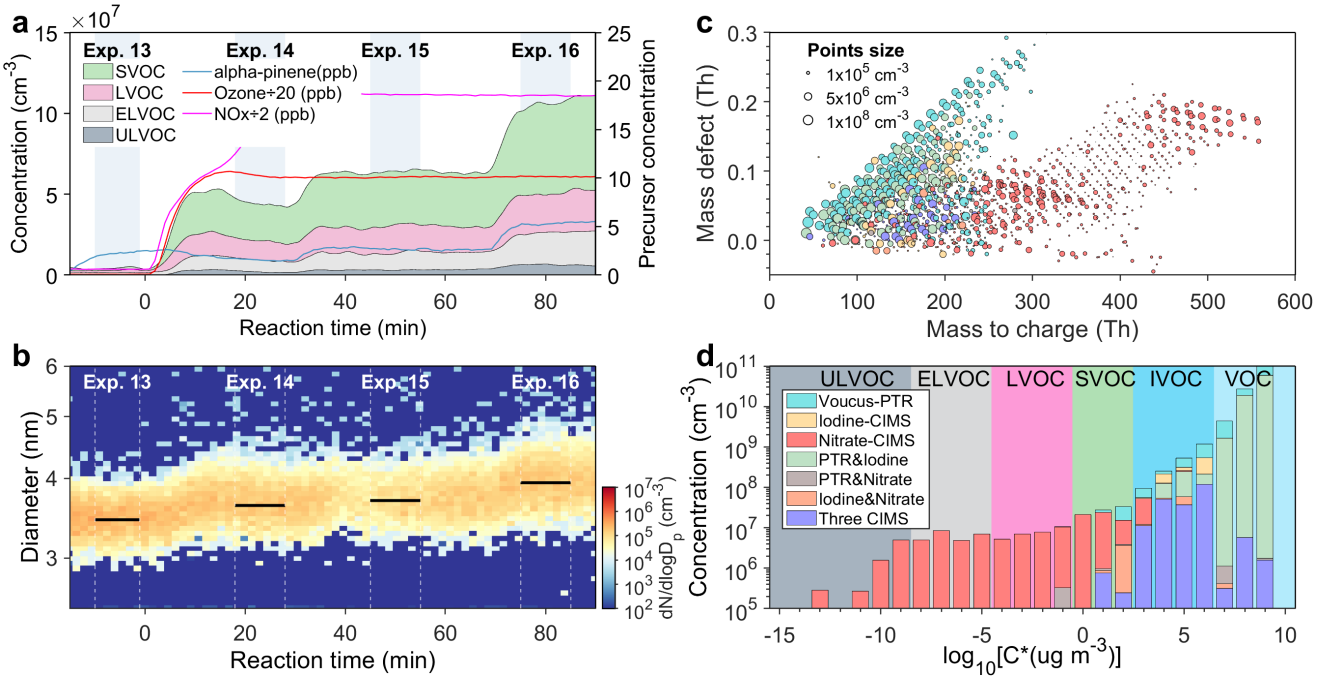


Fig. 13. Particle growth driven by condensation of OOMs formed from α-pinene + O_3 under high NOx conditions (NOx = 44 ppb). a, Profiles of gas-phase precursors and total concentrations of SVOCs, LVOCs, ELVOCs, and ULVOCs during four experiment periods (Exp. 13-16) as highlighted in shaded regions. **b,** Measured PNSDs of Ni-Cr oxide particles at a residence time of 131 s for Exp. 13-16. Vertical dashed white lines mark experimental boundaries, and horizontal black lines indicate the mean mode particle diameter in each experiment. **c,** Mass defect plot for all assigned OOMs in Exp. 16. Marker size scales with OOM's concentration. Marker colors indicate which of the three CIMS (Vocus-PTR, iodine-CIMS, nitrate-CIMS) detected each OOM, including overlaps, following the color scheme in the bottom-right panel. **d,** OOM's concentration as a function of effective saturation concentration ($\log_{10}C^*$), grouped into volatility classes (ULVOC→VOC). Volatility estimates of OOMs are derived using the parametrization of (Zhang et al., 2026). Bars show the concentrations of OOMs detected by at least one of the three CIMS, following the color scheme in the bottom-right panel. Please refer to the main text for quantification rules.

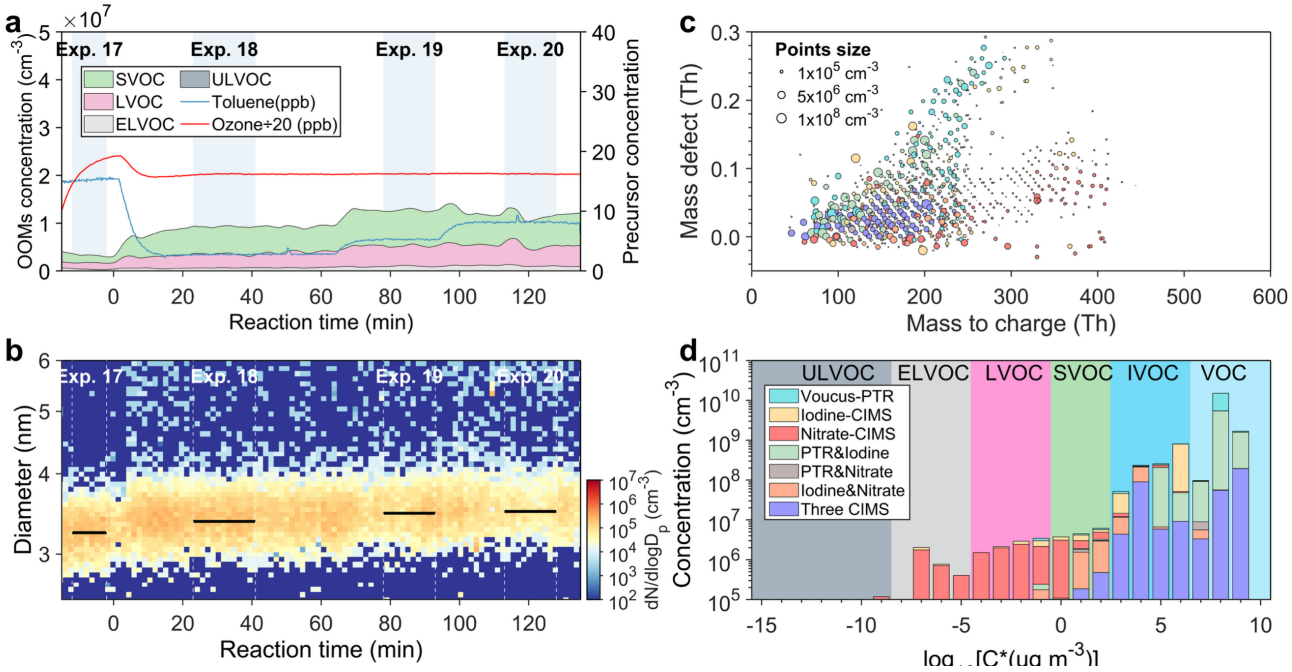


Fig. S14. Particle growth driven by condensation of OOMs formed from toluene + OH under low NOx conditions (NOx<1 ppb). a, Profiles of gas-phase precursors and total concentrations of SVOCs, LVOCs, ELVOCs, and ULVOCs during four experiment periods (Exp. 17-20) as highlighted in shaded regions. **b,** Measured PNSDs of Ni-Cr oxide particles at a residence time of 131 s for Exp. 17-20. Vertical dashed white lines mark experimental boundaries, and horizontal black lines indicate the mean mode particle diameter in each experiment. **c,** Mass defect plot for all assigned OOMs in Exp. 20. Marker size scales with OOM's concentration. Marker colors indicate which of the three CIMS (Vocus-PTR, iodine-CIMS, nitrate-CIMS) detected each OOM, including overlaps, following the color scheme in the bottom-right panel. **d,** OOM's concentration as a function of effective saturation concentration ($\log_{10}C^*$), grouped into volatility classes (ULVOC→VOC). Volatility estimates of OOMs are derived using the parametrization of (Zhang et al., 2026). Bars show the concentrations of OOMs detected by at least one of the three CIMS, following the color scheme in the bottom-right panel. Please refer to the main text for quantification rules.

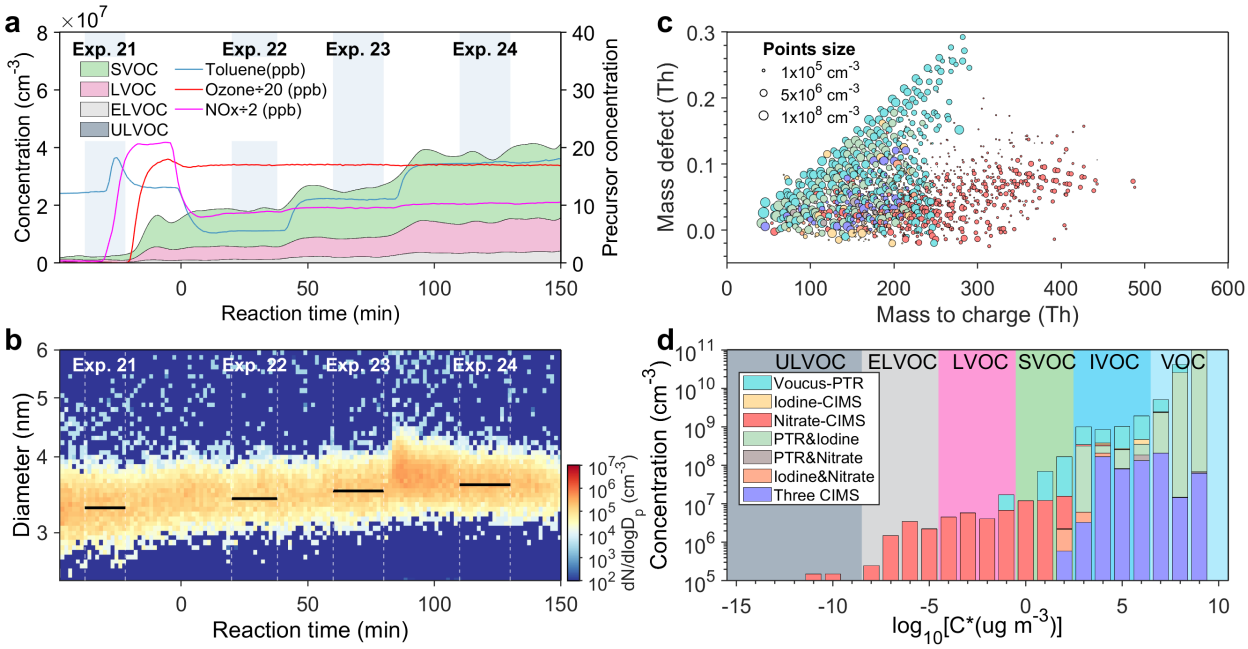


Fig. S15. Particle growth driven by condensation of OOMs formed from toluene +OH under high NOx conditions (NOx=44 ppb). a, Profiles of gas-phase precursors and total concentrations of SVOCs, LVOCs, ELVOCs, and ULVOCs during four experiment periods (Exp. 21-24) as highlighted in shaded regions. **b,** Measured PNSDs of Ni-Cr oxide particles at a residence time of 131 s for Exp. 21-24. Vertical dashed white lines mark experimental boundaries, and horizontal black lines indicate the mean mode particle diameter in each experiment. **c,** Mass defect plot for all assigned OOMs in Exp. 24. Marker size scales with OOM's concentration. Marker colors indicate which of the three CIMS (Vocus-PTR, iodine-CIMS, nitrate-CIMS) detected each OOM, including overlaps, following the color scheme in the bottom-right panel. **d,** OOM's concentration as a function of effective saturation concentration ($\log_{10}$C*), grouped into volatility classes (ULVOC→VOC). Volatility estimates of OOMs are derived using the parametrization of (Zhang et al., 2026). Bars show the concentrations of OOMs detected by at least one of the three CIMS, following the color scheme in the bottom-right panel. Please refer to the main text for quantification rules.

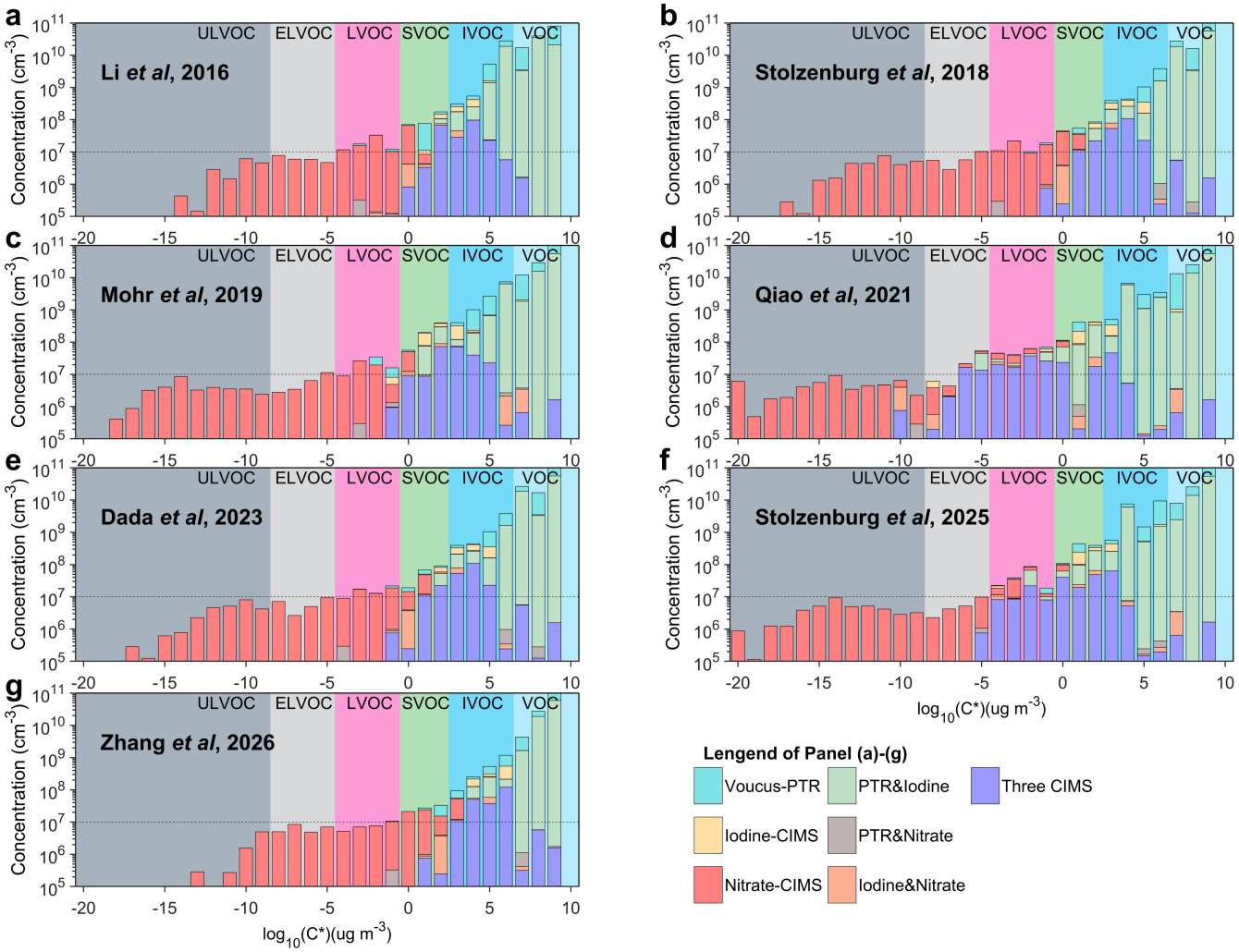


Fig. S16. Comparison of OOMs' volatility distributions derived from seven volatility parametrizations for α-pinene + O_3 under high NOx conditions (NOx = 44ppb) (Exp. 16). Panels (**a-g**) show the effective saturation concentration ($\log_{10}C^*$) distributions of OOMs, calculated using seven volatility parametrizations ((Li et al., 2016); (Stolzenburg et al., 2018); (Mohr et al., 2019); (Qiao et al., 2021); (Dada et al., 2023); (Stolzenburg et al., 2025); and (Zhang et al., 2026), respectively). The colored background indicates volatility classes ranging from ULVOC to VOC. Stacked bars represent the concentrations of OOMs detected by at least one of three CIMS: Vocus-PTR, iodine-CIMS, nitrate-CIMS, Vocus-PTR & iodine-CIMS, iodine-CIMS & nitrate-CIMS, Vocus-PTR & nitrate-CIMS, or three CIMS.

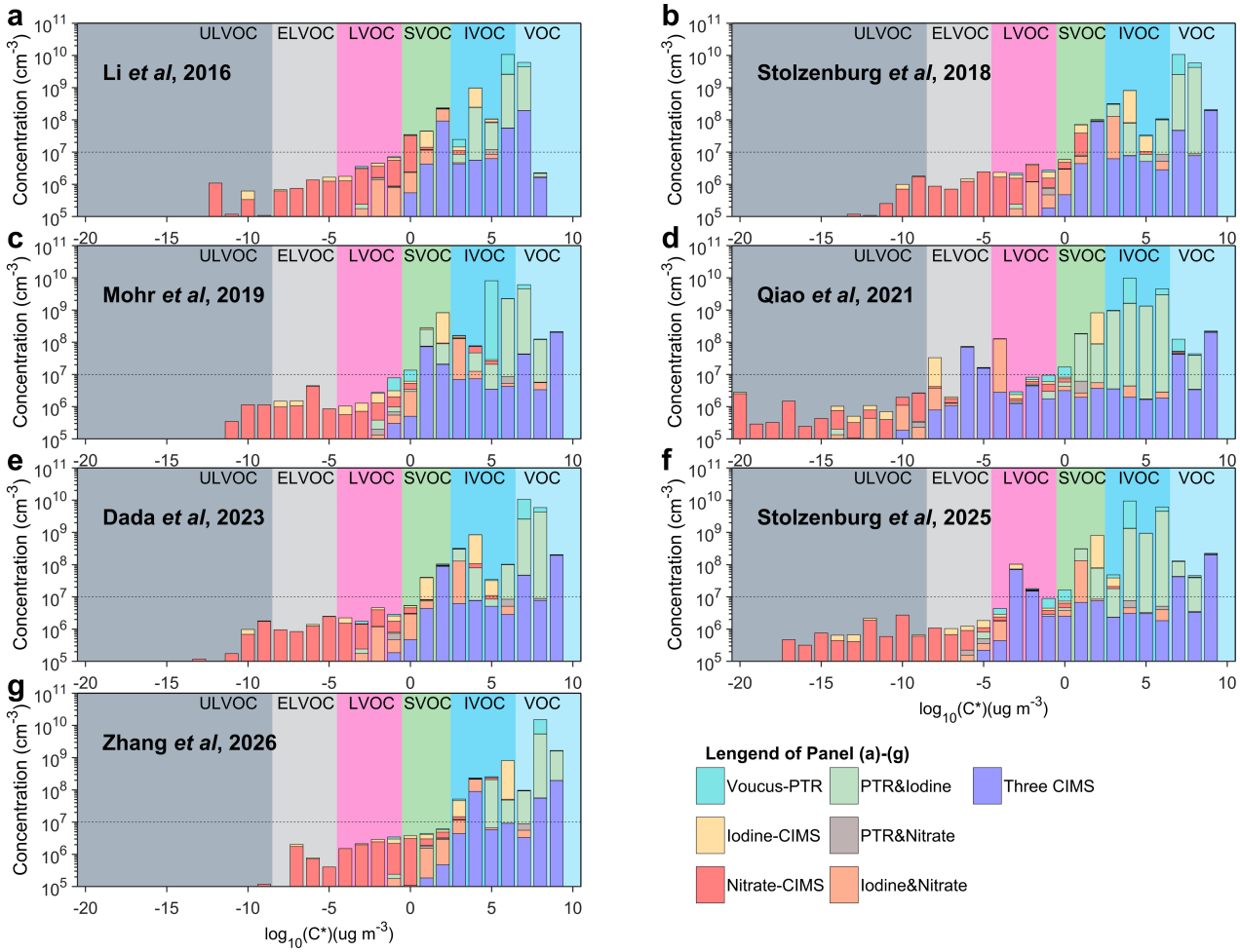


Fig. S17. Comparison of OOM s' volatility distributions derived from seven volatility parametrizations for toluene + OH under low NOx conditions (NOx < 1 ppb) (Exp.20). Panels (**a–g**) show the effective saturation concentration ($\log_{10}C^*$) distributions of OOMs, calculated using seven volatility parametrizations ((Li et al., 2016); (Stolzenburg et al., 2018); (Mohr et al., 2019); (Qiao et al., 2021); (Dada et al., 2023); (Stolzenburg et al., 2025); and (Zhang et al., 2026), respectively). The colored background indicates volatility classes ranging from ULVOC to VOC. Stacked bars represent the concentrations of OOMs detected by at least one of three CIMS: Vocus-PTR, iodine-CIMS, nitrate-CIMS, Vocus-PTR & iodine-CIMS, iodine-CIMS & nitrate-CIMS, Vocus-PTR & nitrate-CIMS, or three CIMS.

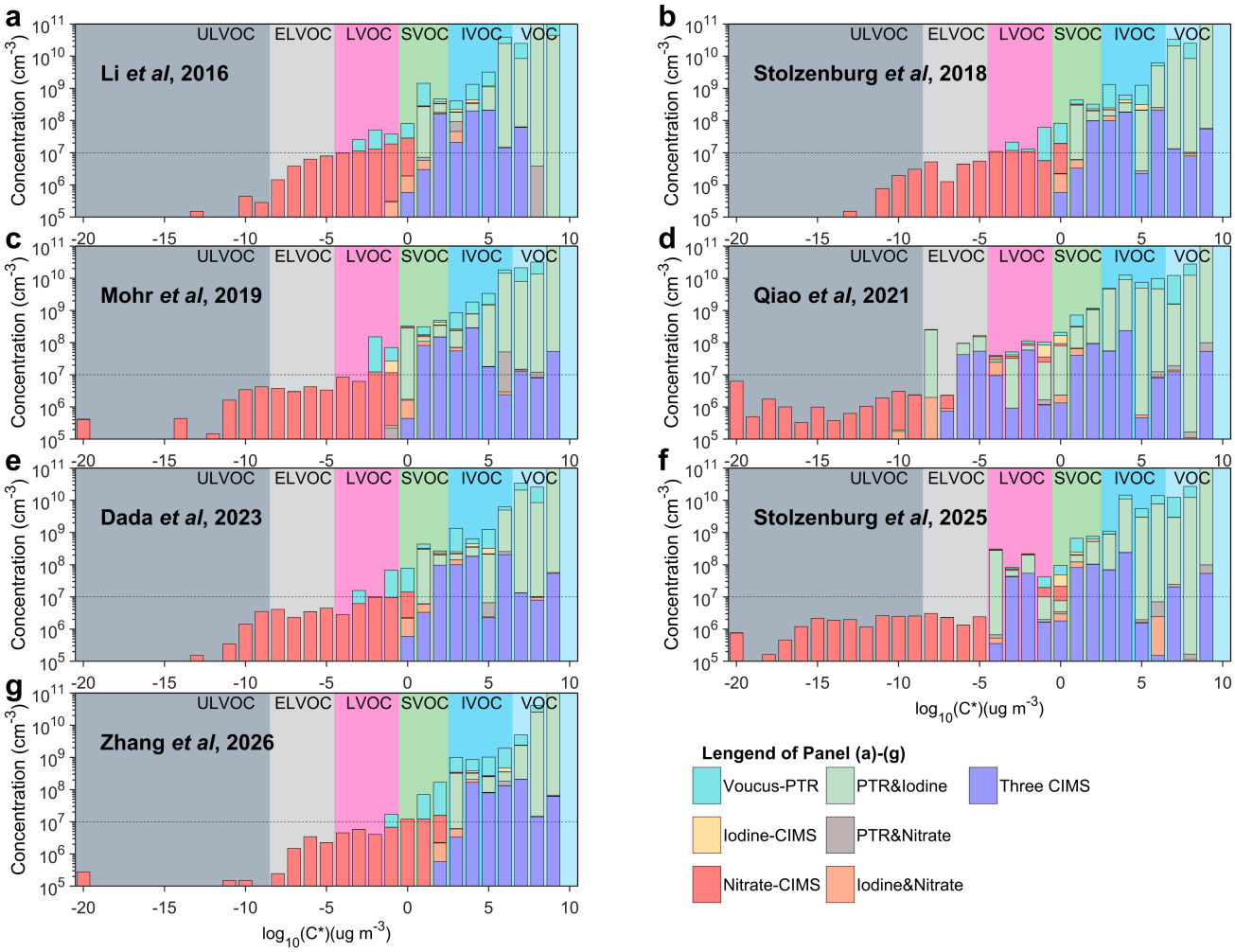


Fig. S18. Comparison of OOMs' volatility distributions derived from seven volatility parametrizations for toluene + OH under high NOx conditions (NOx = 44ppb (Exp.24). Panels (**a–g**) show the effective saturation concentration ($\log_{10}C^*$) distributions of OOMs, calculated using seven volatility parametrizations ((Li et al., 2016); (Stolzenburg et al., 2018); (Mohr et al., 2019); (Qiao et al., 2021); (Dada et al., 2023); (Stolzenburg et al., 2025); and (Zhang et al., 2026), respectively). The colored background indicates volatility classes ranging from ULVOC to VOC. Stacked bars represent the concentrations of OOMs detected by at least one of three CIMS: Vocus-PTR, iodine-CIMS, nitrate-CIMS, Vocus-PTR & iodine-CIMS, iodine-CIMS & nitrate-CIMS, Vocus-PTR & nitrate-CIMS, or three CIMS.

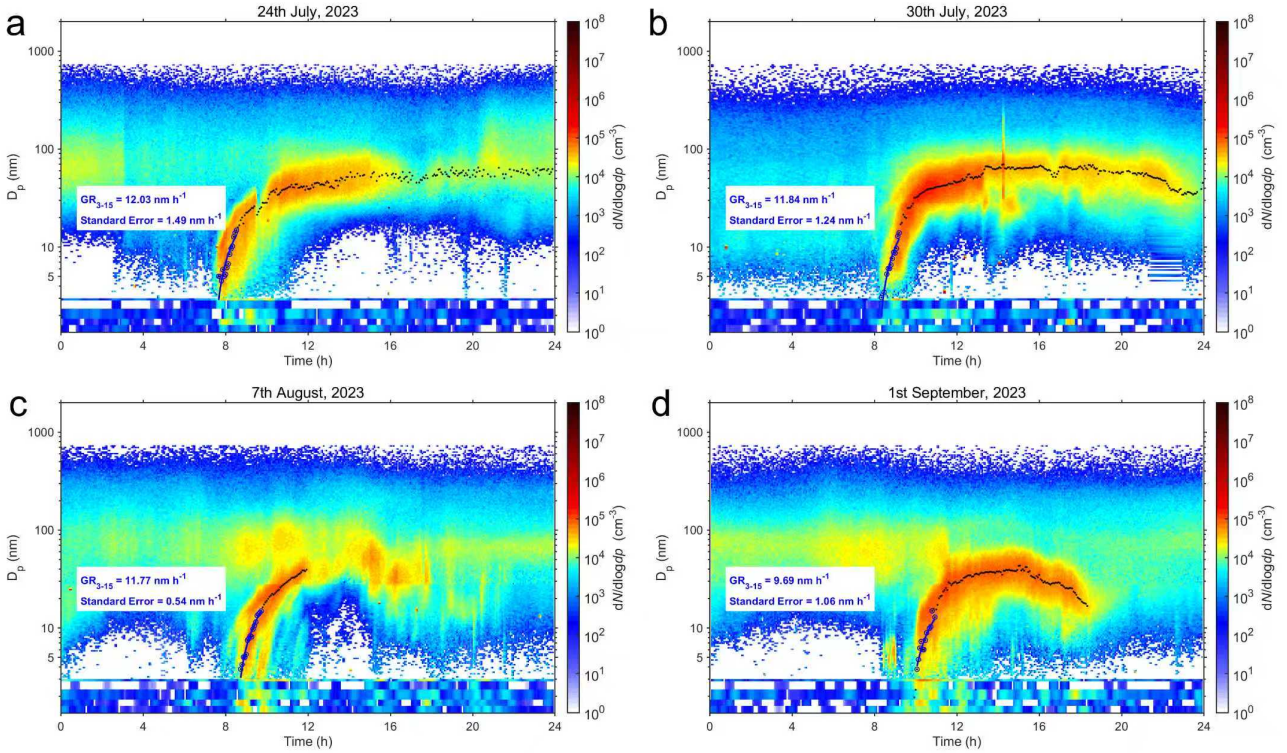


Fig.S19. Observed growth of newly formed particles. Particle number size distributions on (a) 24th July, (b) 30th July, (c) 7th August and (d) 1st September 2023. Blue circles mark the mode diameters used for the fit, and the blue line is the linear fit between 3 and 15 nm. The fitted $GR_{3\text{-}15}$ and its standard error are given in each panel.

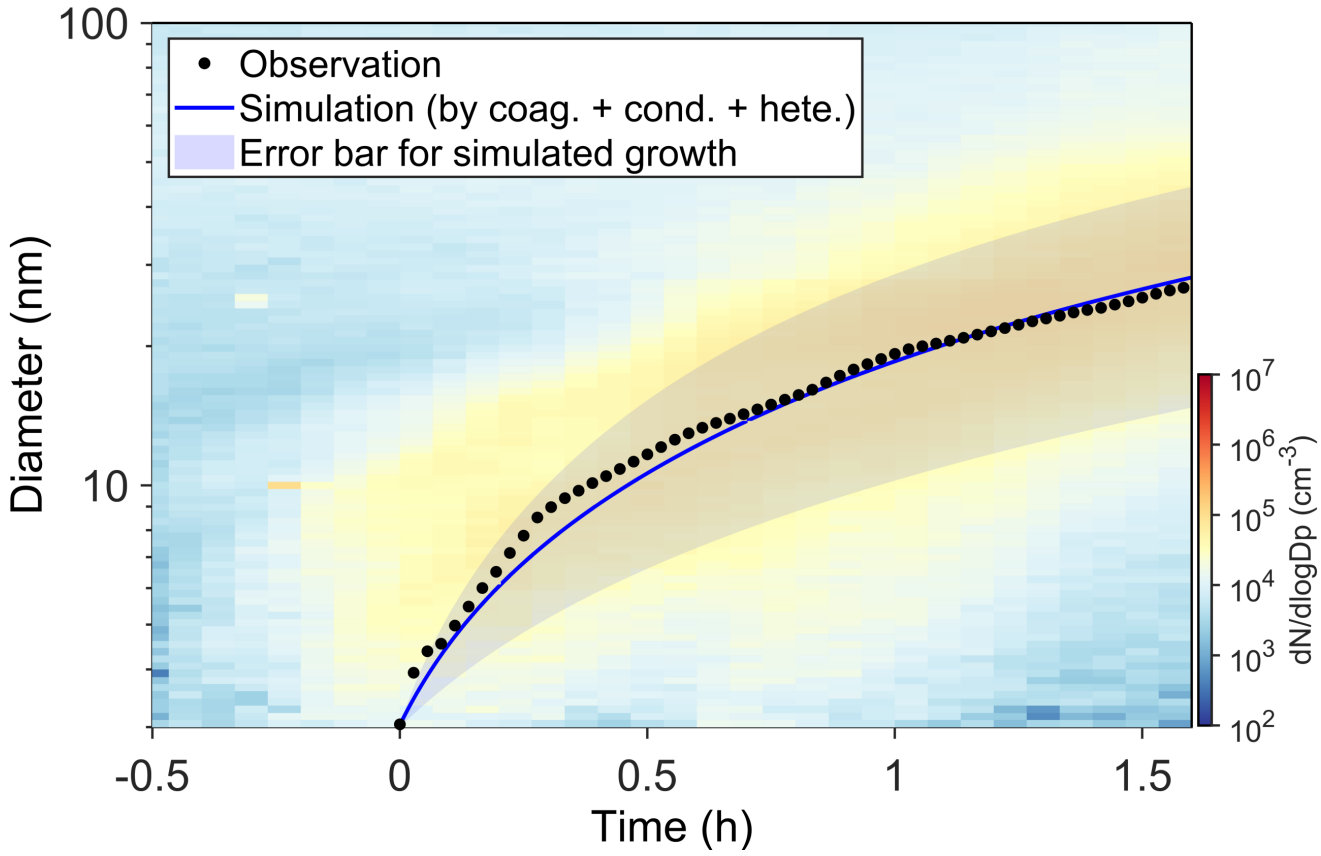


Fig. S20. Comparison of observed and simulated growth of newly formed particles during four NPF events. The colored contour plot shows average PNSDs of four NPF events during the field campaign (4th July to 20th September 2023), with the particle mode diameter of 3 nm in all events serving as the starting point. Black dots represent the observed particle mean mode diameter. The blue line gives the simulated growth resulted from particles coagulation, H_2SO_4 condensation, OOMs' condensation, and heterogeneous reactions, and the light blue shadow denotes the uncertainty of the simulated diameter, combining errors propagated from concentrations of H_2SO_4 and OOM (condensation terms) and heterogeneous reaction.

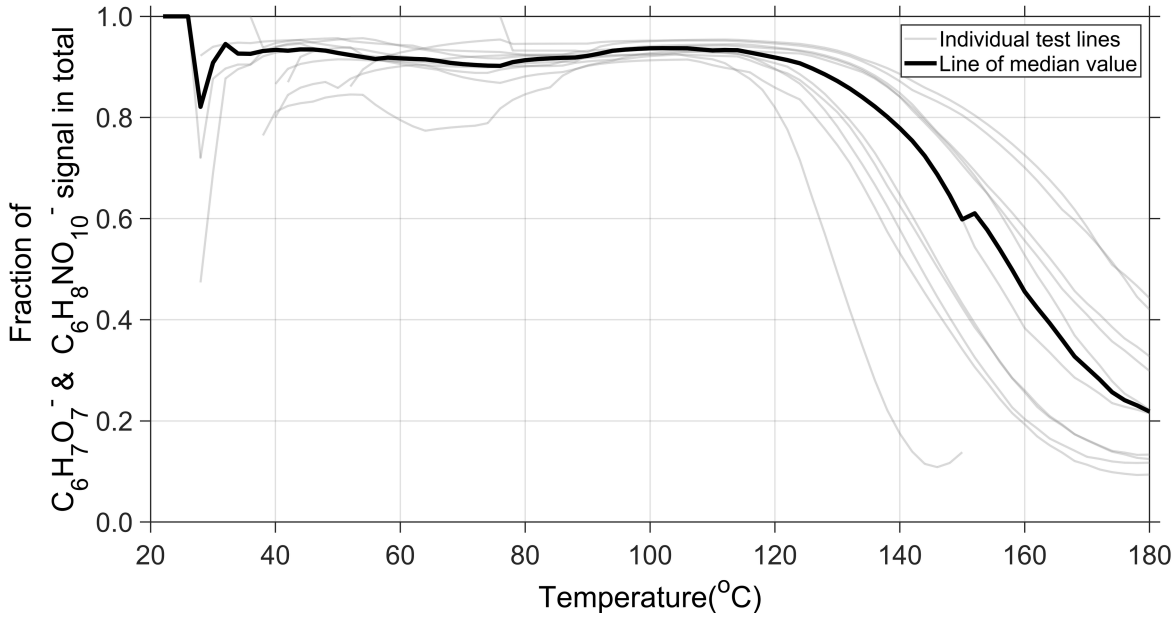


Fig. S21. Potential Thermal decomposition of citric acid. This plot shows the fraction of the ions of citric acid ($C_6H_7O_7^-$ & $C_6H_8NO_{10}^-$) in the total detected signal, including citric acid ($C_6H_7O_7^-$), its cluster with NO_3^- ($C_6H_8NO_{10}^-$), and its thermal decomposition products ($C_5H_5O_5^-$, $C_6H_5O_6^-$, and $C_6H_6NO_9^-$), as a function of temperature as measured by nitrate-CIMS. Thin grey lines represent individual runs, while the thick black line indicates the median of all tests. The $C_6H_7O_7^-$ fraction remains nearly constant below ~120 °C but decreases sharply above 125 °C, marking the onset of thermal decomposition. Accordingly, an experimental desorption temperature between 55 °C and 80 °C was selected to ensure the stability of citric acid.

Exp. NO.	Precursor	Precursor initial concentration (ppb)	Temperature (K)	Relative humidity (%)	NOx (ppb)	O_3 (ppb)	Seed particle diameter (nm)
1-4	Citric acid	$1.6\text{-}8.4\times10^{-3}$	294	<1	<1	<1	3.3
5-8	PEG-7	$1.1\text{-}4.4\times10^{-2}$	293	<1	<1	<1	3.3
9-12	α-pinene	5-20	295	47-51	<1	~95	3.3
13-16	α-pinene	2.5-10	294	47-50	~44	~200	3.3
17-20	Toluene	15-45	296	47-50	<1	~400	3.3
21-24	Toluene	15-45	293	45-53	~44	~400	3.3
25-28	α-pinene	3-10	297	45-48	<1	~95	4.2
29-32	α-pinene	3-10	297	45-48	<1	~95	5.1
33-36	α-pinene	6-24	296	47-49	~45	~200	4.2
37-40	α-pinene	5-20	296	46-49	~45	~200	5.1
41-44	Toluene	15-45	293	43-46	<1	~400	4.2
45-48	Toluene	15-45	295	44-46	<1	~400	5.1
49-52	Toluene	15-45	292	46-52	~42	~400	4.2
53-56	Toluene	18-50	298	46-51	~42	~400	5.1

Table S1. Summary of experimental conditions for organics-driven growth experiments. Listed are the experiment number, precursor for OOMs formation, initial precursor concentration, temperature, relative humidity (RH, %), NOx, ozone (O_3), and the mode diameter of seed particles.

name	formula	M (Th)	Concentration (ppm)	k_{PTR} ($\times 10^{-9}$ cm^3 $molecule^{-1}$ s^{-1})
Methyl Ethyl Ketone	C_4H_8O	72.1064	1.01	3.1642
m-Xylene	C_8H_{10}	106.1672	1.00	2.2419
Benzene	C_6H_6	78.1128	1.01	1.9259
1,2,4-Trimethylbenzene	C_9H_{12}	120.1860	1.02	2.3668
Toluene	C_7H_8	92.1340	1.00	2.0528
α-Pinene	$C_{10}H_{16}$	136.2344	1.04	2.5019

Table S2. Vocus-PTR calibration. This table lists gaseous standards employed for Vocus proton-transfer-reaction mass spectrometer (Vocus-PTR) calibration. For each calibration standard, the chemical name, molecular formula, molar mass, concentration, and proton-transfer reaction rate constants (k_{PTR}) are provided. These compounds represent a range of molar mass and functional groups, ensuring an accurate quantification of oxygenated volatile organic compounds in subsequent measurements.

Name	Formula	M (Th)	Sensitivity (cps/ppt)	dV_{50} (V)
4-Nitrophenol	$C_6H_5NO_3$	139.1088	34.80	8.29
2-Methyl-4-nitrophenol	$C_7H_7NO_3$	152.1354	32.00	8.45
2,6-Dimethyl-4-nitrophenol	$C_8H_9NO_3$	167.1632	34.20	7.38
2-Nitro-1,3- diol	$C_6H_5NO_4$	155.1082	1.25	3.22
2-Methyl-5-nitrophenol	$C_7H_7NO_3$	153.1354	26.10	6.95
2,4-Dinitrophenol	$C_6H_4N_2O_5$	184.1064	3.22	8.37
Nitroethanol	$C_2H_5NO_3$	91.0660	12.50	4.67
Nitroglycerin (Glyceryl trinitrate)	$C_3H_5N_3O_9$	227.0865	28.30	8.00
Isosorbide mononitrate	$C_6H_9NO_6$	191.1388	15.00	5.68
Isosorbide dinitrate	$C_6H_8N_2O_8$	236.1363	24.10	6.10
Acetonitrile	CH_3CN	41.0519	8.40×10^{-4}	2.35
Water	H_2O	18.0153	3.73×10^{-8}	1.85

Table S3. Declustering-voltage (dV_{50}) scans with I-CIMS. This table lists gaseous standards selected to characterize the ion–molecule declustering behavior in iodine chemical ionization mass spectrometer (I-CIMS). For each calibrant, the chemical name, molecular formula, molar mass, instrument sensitivity, and the half-signal declustering voltage (dV_{50}) are provided. Calibrants with different molecular weights and functional groups were chosen to cover a broad range of binding strengths between analyte I^- clusters, enabling a reliable calibration of the instrument's declustering voltage response.

Parameterization	Derivation basis	Required inputs	Intended application	Behaviour in this study
Li et al. (2016)	Large dataset of organic compounds (>3×10^4 species) spanning CH, CHO, CHN, CHON and CHOS classes, with vapour pressures from measurements and group-contribution estimates; not specific to autoxidation products	nC, nO, nN (class-specific coefficient sets)	General volatility estimation across a broad SOA compound space ("molecular corridors")	Reproduced GRs under low NOx; overpredicted under high NO_x, most strongly for toluene + OH
Stolzenburg et al. (2018)	α-Pinene-derived HOMs generated in the CLOUD chamber; formulation adjusted to reproduce nanoparticle growth between −50 and +25 °C	nC, nO; explicit temperature dependence	Biogenic nucleation and early growth across a wide tropospheric temperature range	Reproduced GRs under low NO_x; overpredicted under high NOx
Mohr et al. (2019)	FIGAERO-CIMS measurements-derived volatilities of α-pinene oxidation products (boreal forest and chamber measurements); revision of Donahue et al. (2011)'s formulation with a modified oxygen term	nC, nO	HOMs-driven nanoparticle growth in BVOCs-dominated boreal environments	Reproduced GRs under low NO_x; overpredicted under high NOx
Qiao et al. (2021)	Revision from Mohr et al. (2019), extended to the OOM population observed in urban Beijing, including N-containing species	nC, nO, nN	OOM contribution to the growth of newly formed particles in urban environments	Systematically overpredicted growth across all precursor and NOx conditions
Dada et al. (2023)	Sesquiterpene (C15H24) and monoterpene oxidation products generated at CLOUD chamber	nC, nO, nN	Biogenic new particle formation including sesquiterpene oxidation	Reproduced GRs under low NOx; overpredicted under high NOx
Stolzenburg et al. (2025)	Formulation refined against autoxidation products from biogenic VOCs, developed in the context of nanoparticle mass-closure analysis	nC, nO, nN	Mass closure of nanoparticle growth in BVOC-dominated environments	Systematically overpredicted growth across all precursor and NOx conditions
Zhang et al. (2026)	Volatility measurements by FIGAERO-iodide-CIMS of ambient particulate OOMs from urban and suburban sites in eastern China (mixed anthropogenic–biogenic environment with high NOx)	nC, nO, nN	Ambient OOMs in polluted, NOx-influenced environments	Best agreement with measured GRs in all laboratory experiments; slight underprediction of ambient GR at Lake Tai

Table S4. Inter-comparison of the seven OOM volatility parameterizations evaluated in our study. *n*C, *n*O and *n*N denote the numbers of carbon, oxygen and nitrogen atoms in the molecular formula of OOMs.

Name	Date	Concentrations (ppb)	Source
N_2O_5	Campaign average	3.4×10^{-4}	WRF-CMAQ simulation
NO_2	July 24th, 2023	3.2	Measurements at Lake Tai
	July 30th, 2023	3.8	
	August 7th, 2023	11.8	
	September 1st, 2023	10.1	
$NO_3\cdot$	Campaign average	2.0×10^{-2}	Common parameter 5×10^{8} cm^{-3}
HNO_3	Campaign average	0.8	WRF-CMAQ simulation
Organic nitrates	Campaign average	0.4	WRF-CMAQ simulation
IEPOX	July 24th, 2023	4.7×10-2	PTR at Lake Tai
	July 30th, 2023	5.1×10-2	
	August 7th, 2023	6.7×10-2	
	September 1st, 2023	6.1×10-2	
IMAE	July 24th, 2023	2.1×10-2	PTR at Lake Tai
	July 30th, 2023	2.8×10-2	
	August 7th, 2023	4.0×10-2	
	September 1st, 2023	2.2×10-2	
GLY	Campaign average	0.2	WRF-CMAQ simulation
MGLY	Campaign average	9.6×10^{-2}	WRF-CMAQ simulation
Temperature	July 24th, 2023	301K	Lake Tai
	July 30th, 2023	300K	
	August 7th, 2023	303K	
	September 1st, 2023	296K	

Table S5. Gas-phase species used in heterogeneous reaction simulations for the four NPF events. This table summarizes the gaseous compounds and their corresponding concentrations applied in the model simulations of heterogeneous reactions. The listed species include key inorganic oxidants, organic nitrates, and representative reactive organic vapors such as IEPOX, IMAE, GLY, and MGLY.

Parameter	Value	Unit
Pressure	101325	Pa
Water vapor mixing ratio	0.01	/
Air density	1.225	kg/m^3
H^+ concentration	1×10^{-4}	mol/L
HSO_4^- concentration	1×10^{-6}	mol/L
Sulfate Concentration	5	$\mu g/m^3$
Liquid water content	5	$\mu g/m^3$
Nitrate concentration	5	$\mu g/m^3$

Table S6. Environmental parameters used in model simulations of heterogeneous reactions. This table lists environmental parameters applied in the model simulations of heterogeneous reactions, including thermodynamic conditions and chemical composition of particles. The aqueous-phase ionic concentrations (H^+, HSO_4^-) and aerosol components (sulfate, nitrate, and liquid water content) were set to represent typical urban atmospheric conditions at 101325 Pa, ensuring consistency between observation and model.

References

An, J., Huang, Y., Huang, C., Wang, X., Yan, R., Wang, Q., Wang, H., Jing, S., Zhang, Y., Liu, Y., Chen, Y., Xu, C., Qiao, L., Zhou, M., Zhu, S., Hu, Q., Lu, J., and Chen, C.: Emission inventory of air pollutants and chemical speciation for specific anthropogenic sources based on local measurements in the Yangtze River Delta region, China, Atmos. Chem. Phys., 21, 2003–2025, https://doi.org/10.5194/acp-21-2003-2021, 2021.

An, J., Huang, C., Huang, D., Qin, M., Liu, H., Yan, R., Qiao, L., Zhou, M., Li, Y., Zhu, S., Wang, Q., and Wang, H.: Sources of organic aerosols in eastern China: a modeling study with high-resolution intermediate-volatility and semivolatile organic compound emissions, Atmos. Chem. Phys., 23, 323–344, https://doi.org/10.5194/acp-23-323-2023, 2022.

Attoui, M.: Mobility distributions of Sub 5 nm singly self-charged water soluble and non-soluble particles from a heated NiCr wire in clean dry air, Aerosol Sci. Technol., 56, 859–868, https://doi.org/10.1080/02786826.2022.2095892, 2022.

Bianchi, F., Kurtén, T., Riva, M., Mohr, C., Rissanen, M. P., Roldin, P., Berndt, T., Crounse, J. D., Wennberg, P. O., Mentel, T. F., Wildt, J., Junninen, H., Jokinen, T., Kulmala, M., Worsnop, D. R., Thornton, J. A., Donahue, N., Kjaergaard, H. G., and Ehn, M.: Highly Oxygenated Organic Molecules (HOM) from Gas-Phase Autoxidation Involving Peroxy Radicals: A Key Contributor to Atmospheric Aerosol, Chem. Rev., 119, 3472–3509, https://doi.org/10.1021/acs.chemrev.8b00395, 2019.

Carbone, F., Attoui, M., and Gomez, A.: Challenges of measuring nascent soot in flames as evidenced by high-resolution differential mobility analysis, Aerosol Sci. Tech., 50, 740–757, https://doi.org/10.1080/02786826.2016.1179715, 2016.

Dada, L., Stolzenburg, D., Simon, M., Fischer, L., Heinritzi, M., Wang, M., Xiao, M., Vogel, A. L., Ahonen, L., Amorim, A., Baalbaki, R., Baccarini, A., Baltensperger, U., Bianchi, F., Daellenbach, K. R., DeVivo, J., Dias, A., Dommen, J., Duplissy, J., Finkenzeller, H., Hansel, A., He, X.-C., Hofbauer, V., Hoyle, C. R., Kangasluoma, J., Kim, C., Kürten, A., Kvashnin, A., Mauldin, R., Makhmutov, V., Marten, R., Mentler, B., Nie, W., Petäjä, T., Quéléver, L. L. J., Saathoff, H., Tauber, C., Tome, A., Molteni, U., Volkamer, R., Wagner, R., Wagner, A. C., Wimmer, D., Winkler, P. M., Yan, C., Zha, Q., Rissanen, M., Gordon, H., Curtius, J., Worsnop, D. R., Lehtipalo, K., Donahue, N. M., Kirkby, J., Haddad, I. E., and Kulmala, M.: Role of sesquiterpenes in biogenic new particle formation, Sci. Adv., 9, eadi5297, https://doi.org/10.1126/sciadv.adi5297, 2023.

Donahue, N. M., Epstein, S. A., Pandis, S. N., and Robinson, A. L.: A two-dimensional volatility basis set: 1. organic-aerosol mixing thermodynamics, Atmos. Chem. Phys., 11, 3303–3318, https://doi.org/10.5194/acp-11-3303-2011, 2011.

Fang, J., Wang, Y., Attoui, M., Chadha, T. S., Ray, J. R., Wang, W.-N., Jun, Y.-S., and Biswas, P.: Measurement of Sub-2 nm Clusters of Pristine and Composite Metal Oxides during Nanomaterial Synthesis in Flame Aerosol Reactors, Anal. Chem., 86, 7523–7529, https://doi.org/10.1021/ac5012816, 2014.

Fomenko, E., Altman, I., Boskovic, L., and Agranovski, I. E.: Nanoparticle Generation in Glowing Wire Generator: Insight into Nucleation Peculiarities, Materials, 14, 7775, https://doi.org/10.3390/ma14247775, 2021.

Fountoukis, C. and Nenes, A.: ISORROPIA II: a computationally efficient thermodynamic equilibrium model for K^+–Ca^{2+}–Mg^{2+}–NH_4^+–Na^+–SO_4^{2-}–NO_3^-–Cl^-–H_2O aerosols, Atmos. Chem. Phys., 7, 4639–4659, https://doi.org/10.5194/acp-7-4639-2007, 2007.

Garmash, O., Kumar, A., Jha, S., Barua, S., Hyttinen, N., Iyer, S., and Rissanen, M.: Enhanced detection of aromatic oxidation products using NO 3 − chemical ionization mass spectrometry with limited nitric acid, Environ. Sci.: Atmos., 4, 1368–1381, https://doi.org/10.1039/d4ea00087k, 2024.

Guenther, A., Karl, T., Harley, P., Wiedinmyer, C., Palmer, P. I., and Geron, C.: Estimates of global terrestrial isoprene emissions using MEGAN (Model of Emissions of Gases and Aerosols from Nature), Atmos. Chem. Phys., 6, 3181–3210, https://doi.org/10.5194/acp-6-3181-2006, 2006.

Hanson, D. R., Ravishankara, A. R., and Solomon, S.: Heterogeneous reactions in sulfuric acid aerosols: A framework for model calculations, J. Geophys. Res.: Atmos., 99, 3615–3629, https://doi.org/10.1029/93jd02932, 1994.

Heinritzi, M., Simon, M., Steiner, G., Wagner, A. C., Kürten, A., Hansel, A., and Curtius, J.: Characterization of the mass-dependent transmission efficiency of a CIMS, Atmos. Meas. Tech., 9, 1449–1460, https://doi.org/10.5194/amt-9-1449-2016, 2016.

Hoppel, W. A. and Frick, G. M.: Ion—Aerosol Attachment Coefficients and the Steady-State Charge Distribution on Aerosols in a Bipolar Ion Environment, Aerosol Sci. Technol., 5, 1–21, https://doi.org/10.1080/02786828608959073, 1986.

Isaacman-VanWertz, G., Massoli, P., O'Brien, R. E., Nowak, J. B., Canagaratna, M. R., Jayne, J. T., Worsnop, D. R., Su, L., Knopf, D. A., Misztal, P. K., Arata, C., Goldstein, A. H., and Kroll, J. H.: Using advanced mass spectrometry techniques to fully characterize atmospheric organic carbon: current capabilities and remaining gaps, Faraday Discuss., 200, 579–598, https://doi.org/10.1039/c7fd00021a, 2017.

Jokinen, T., Sipilä, M., Junninen, H., Ehn, M., Lönn, G., Hakala, J., Petäjä, T., III, R. L. M., Kulmala, M., and Worsnop, D. R.: Atmospheric sulphuric acid and neutral cluster measurements using CI-APi-TOF, Atmos. Chem. Phys., 12, 4117–4125, https://doi.org/10.5194/acp-12-4117-2012, 2012.

Kallinger, P. and Szymanski, W. W.: Experimental determination of the steady-state charging probabilities and particle size conservation in non-radioactive and radioactive bipolar aerosol chargers in the size range of 5–40 nm, J. Nanoparticle Res., 17, 171, https://doi.org/10.1007/s11051-015-2981-x, 2015.

Krechmer, J., Lopez-Hilfiker, F., Koss, A., Hutterli, M., Stoermer, C., Deming, B., Kimmel, J., Warneke, C., Holzinger, R., Jayne, J., Worsnop, D., Fuhrer, K., Gonin, M., and Gouw, J. de: Evaluation of a New Reagent-Ion Source and Focusing Ion–

Molecule Reactor for Use in Proton-Transfer-Reaction Mass Spectrometry, Anal. Chem., 90, 12011–12018, https://doi.org/10.1021/acs.analchem.8b02641, 2018.

Kürten, A., Rondo, L., Ehrhart, S., and Curtius, J.: Calibration of a Chemical Ionization Mass Spectrometer for the Measurement of Gaseous Sulfuric Acid, J. Phys. Chem., 116, 6375–6386, https://doi.org/10.1021/jp212123n, 2012.

Li, H., Almeida, T. G., Luo, Y., Zhao, J., Palm, B. B., Daub, C. D., Huang, W., Mohr, C., Krechmer, J. E., Kurtén, T., and Ehn, M.: Fragmentation inside proton-transfer-reaction-based mass spectrometers limits the detection of ROOR and ROOH peroxides, Atmos. Meas. Tech., 15, 1811–1827, https://doi.org/10.5194/amt-15-1811-2022, 2022.

Li, Y., Pöschl, U., and Shiraiwa, M.: Molecular corridors and parameterizations of volatility in the chemical evolution of organic aerosols, Atmos. Chem. Phys., 16, 3327–3344, https://doi.org/10.5194/acp-16-3327-2016, 2016.

Liu, H., Meng, Z.-H., Lv, Z.-F., Wang, X.-T., Deng, F.-Y., Liu, Y., Zhang, Y.-N., Shi, M.-S., Zhang, Q., and He, K.-B.: Emissions and health impacts from global shipping embodied in US–China bilateral trade, Nat. Sustain., 2, 1027–1033, https://doi.org/10.1038/s41893-019-0414-z, 2019.

Liu, Y., Attoui, M., Yang, K., Chen, J., Li, Q., and Wang, L.: Size-resolved chemical composition analysis of ions produced by a commercial soft X-ray aerosol neutralizer, J. Aerosol. Sci., 147, 105586, https://doi.org/10.1016/j.jaerosci.2020.105586, 2020.

Lopez-Hilfiker, F. D., Iyer, S., Mohr, C., Lee, B. H., D'Ambro, E. L., Kurtén, T., and Thornton, J. A.: Constraining the sensitivity of iodide adduct chemical ionization mass spectrometry to multifunctional organic molecules using the collision limit and thermodynamic stability of iodide ion adducts, Atmos. Meas. Tech., 9, 1505–1512, https://doi.org/10.5194/amt-9-1505-2016, 2016.

Mohr, C., Thornton, J. A., Heitto, A., Lopez-Hilfiker, F. D., Lutz, A., Riipinen, I., Hong, J., Donahue, N. M., Hallquist, M., Petäjä, T., Kulmala, M., and Yli-Juuti, T.: Molecular identification of organic vapors driving atmospheric nanoparticle growth, Nat. Commun., 10, 4442, https://doi.org/10.1038/s41467-019-12473-2, 2019.

Picard, D., Attoui, M., and Sellegri, K.: B3010: a boosted TSI 3010 condensation particle counter for airborne studies, Atmos. Meas. Tech., 12, 2531–2543, https://doi.org/10.5194/amt-12-2531-2019, 2019.

Pye, H. O. T., Pinder, R. W., Piletic, I. R., Xie, Y., Capps, S. L., Lin, Y.-H., Surratt, J. D., Zhang, Z., Gold, A., Luecken, D. J., Hutzell, W. T., Jaoui, M., Offenberg, J. H., Kleindienst, T. E., Lewandowski, M., and Edney, E. O.: Epoxide Pathways Improve Model Predictions of Isoprene Markers and Reveal Key Role of Acidity in Aerosol Formation, Environ. Sci. Technol., 47, 11056–11064, https://doi.org/10.1021/es402106h, 2013.

Qiao, X., Yan, C., Li, X., Guo, Y., Yin, R., Deng, C., Li, C., Nie, W., Wang, M., Cai, R., Huang, D., Wang, Z., Yao, L., Worsnop, D. R., Bianchi, F., Liu, Y., Donahue, N. M., Kulmala, M., and Jiang, J.: Contribution of Atmospheric Oxygenated

Organic Compounds to Particle Growth in an Urban Environment, Environ. Sci. Technol., 55, 13646–13656, https://doi.org/10.1021/acs.est.1c02095, 2021.

Riva, M., Rantala, P., Krechmer, J. E., Peräkylä, O., Zhang, Y., Heikkinen, L., Garmash, O., Yan, C., Kulmala, M., Worsnop, D., and Ehn, M.: Evaluating the performance of five different chemical ionization techniques for detecting gaseous oxygenated organic species, Atmos. Meas. Tech., 12, 2403–2421, https://doi.org/10.5194/amt-12-2403-2019, 2019.

Sekimoto, K., Li, S.-M., Yuan, B., Koss, A., Coggon, M., Warneke, C., and Gouw, J. de: Calculation of the sensitivity of proton-transfer-reaction mass spectrometry (PTR-MS) for organic trace gases using molecular properties, Int. J. Mass Spectrom., 421, 71–94, https://doi.org/10.1016/j.ijms.2017.04.006, 2017.

Shi, G., Xu, J., Shi, X., Liu, B., Bi, X., Xiao, Z., Chen, K., Wen, J., Dong, S., Tian, Y., Feng, Y., Yu, H., Song, S., Zhao, Q., Gao, J., and Russell, A. G.: Aerosol pH Dynamics During Haze Periods in an Urban Environment in China: Use of Detailed, Hourly, Speciated Observations to Study the Role of Ammonia Availability and Secondary Aerosol Formation and Urban Environment, J. Geophys. Res.: Atmos., 124, 9730–9742, https://doi.org/10.1029/2018jd029976, 2019.

Song, S., Gao, M., Xu, W., Sun, Y., Worsnop, D. R., Jayne, J. T., Zhang, Y., Zhu, L., Li, M., Zhou, Z., Cheng, C., Lv, Y., Wang, Y., Peng, W., Xu, X., Lin, N., Wang, Y., Wang, S., Munger, J. W., Jacob, D. J., and McElroy, M. B.: Possible heterogeneous chemistry of hydroxymethanesulfonate (HMS) in northern China winter haze, Atmos. Chem. Phys., 19, 1357–1371, https://doi.org/10.5194/acp-19-1357-2019, 2019.

Stolzenburg, D., Fischer, L., Vogel, A. L., Heinritzi, M., Schervish, M., Simon, M., Wagner, A. C., Dada, L., Ahonen, L. R., Amorim, A., Baccarini, A., Bauer, P. S., Baumgartner, B., Bergen, A., Bianchi, F., Breitenlechner, M., Brilke, S., Mazon, S. B., Chen, D., Dias, A., Draper, D. C., Duplissy, J., Haddad, I. E., Finkenzeller, H., Frege, C., Fuchs, C., Garmash, O., Gordon, H., He, X., Helm, J., Hofbauer, V., Hoyle, C. R., Kim, C., Kirkby, J., Kontkanen, J., Kürten, A., Lampilahti, J., Lawler, M., Lehtipalo, K., Leiminger, M., Mai, H., Mathot, S., Mentler, B., Molteni, U., Nie, W., Nieminen, T., Nowak, J. B., Ojdanic, A., Onnela, A., Passananti, M., Petäjä, T., Quéléver, L. L. J., Rissanen, M. P., Sarnela, N., Schallhart, S., Tauber, C., Tomé, A., Wagner, R., Wang, M., Weitz, L., Wimmer, D., Xiao, M., Yan, C., Ye, P., Zha, Q., Baltensperger, U., Curtius, J., Dommen, J., Flagan, R. C., Kulmala, M., Smith, J. N., Worsnop, D. R., Hansel, A., Donahue, N. M., and Winkler, P. M.: Rapid growth of organic aerosol nanoparticles over a wide tropospheric temperature range, Proc. Nati. Acad. Sci. U.S.A., 115, 201807604, https://doi.org/10.1073/pnas.1807604115, 2018.

Stolzenburg, D., Wang, M., Schervish, M., and Donahue, N. M.: Tutorial: Dynamic organic growth modeling with a volatility basis set, J. Aerosol Sci., 166, 106063, https://doi.org/10.1016/j.jaerosci.2022.106063, 2022.

Stolzenburg, D., Sarnela, N., Bianchi, F., Cai, J., Cai, R., Cheng, Y., Dada, L., Donahue, N. M., Grothe, H., Holm, S., Kerminen, V.-M., Lehtipalo, K., Petäjä, T., Sulo, J., Winkler, P. M., Yan, C., Kangasluoma, J., and Kulmala, M.: Incomplete mass closure in atmospheric nanoparticle growth, npj Clim. Atmos. Sci., 8, 75, https://doi.org/10.1038/s41612-025-00893-5, 2025.

Tröstl, J., Chuang, W. K., Gordon, H., Heinritzi, M., Yan, C., Molteni, U., Ahlm, L., Frege, C., Bianchi, F., Wagner, R., Simon, M., Lehtipalo, K., Williamson, C., Craven, J. S., Duplissy, J., Adamov, A., Almeida, J., Bernhammer, A.-K., Breitenlechner, M., Brilke, S., Dias, A., Ehrhart, S., Flagan, R. C., Franchin, A., Fuchs, C., Guida, R., Gysel, M., Hansel, A., Hoyle, C. R., Jokinen, T., Junninen, H., Kangasluoma, J., Keskinen, H., Kim, J., Krapf, M., Kürten, A., Laaksonen, A., Lawler, M., Leiminger, M., Mathot, S., Möhler, O., Nieminen, T., Onnela, A., Petäjä, T., Piel, F. M., Miettinen, P., Rissanen, M. P., Rondo, L., Sarnela, N., Schobesberger, S., Sengupta, K., Sipilä, M., Smith, J. N., Steiner, G., Tomè, A., Virtanen, A., Wagner, A. C., Weingartner, E., Wimmer, D., Winkler, P. M., Ye, P., Carslaw, K. S., Curtius, J., Dommen, J., Kirkby, J., Kulmala, M., Riipinen, I., Worsnop, D. R., Donahue, N. M., and Baltensperger, U.: The role of low-volatility organic compounds in initial particle growth in the atmosphere, Nature, 533, 527–531, https://doi.org/10.1038/nature18271, 2016.

Wang, Y., Yang, G., Lu, Y., Liu, Y., Chen, J., and Wang, L.: Detection of gaseous dimethylamine using vocus proton-transfer-reaction time-of-flight mass spectrometry, Atmos. Environ., 243, 117875, https://doi.org/10.1016/j.atmosenv.2020.117875, 2020.

Yao, L., Garmash, O., Bianchi, F., Zheng, J., Yan, C., Kontkanen, J., Junninen, H., Mazon, S. B., Ehn, M., Paasonen, P., Sipilä, M., Wang, M., Wang, X., Xiao, S., Chen, H., Lu, Y., Zhang, B., Wang, D., Fu, Q., Geng, F., Li, L., Wang, H., Qiao, L., Yang, X., Chen, J., Kerminen, V.-M., Petäjä, T., Worsnop, D. R., Kulmala, M., and Wang, L.: Atmospheric new particle formation from sulfuric acid and amines in a Chinese megacity, Science, 361, 278–281, https://doi.org/10.1126/science.aao4839, 2018.

Zhang, X., Li, C., Xue, S., Yang, X., Wang, Y., Li, Y., Cai, R., Yao, L., and Wang, L.: Volatility Parametrization of Atmospheric Organic Compounds Based on Molecular Formula, ACS EST Air, 3, 291–301, https://doi.org/10.1021/acsestair.5c00167, 2026.

Zhang, Y., Wang, Y., Li, C., Li, Y., Yin, S., Claflin, M. S., Lerner, B. M., Worsnop, D., and Wang, L.: Interpretation of mass spectra by a Vocus proton-transfer-reaction mass spectrometer (PTR-MS) at an urban site: insights from gas chromatographic pre-separation, Atmos. Meas. Tech., 18, 3547–3568, https://doi.org/10.5194/amt-18-3547-2025, 2025.

Zheng, B., Zhang, Q., Zhang, Y., He, K. B., Wang, K., Zheng, G. J., Duan, F. K., Ma, Y. L., and Kimoto, T.: Heterogeneous chemistry: a mechanism missing in current models to explain secondary inorganic aerosol formation during the January 2013 haze episode in North China, Atmos. Chem. Phys., 15, 2031–2049, https://doi.org/10.5194/acp-15-2031-2015, 2015.